INTERNATIONAL ATOMIC ENERGY AGENCY
UNITED NATIONS EDUCATIONAL, SCIENTIFIC AND CULTURAL ORGANIZATION

INTERNATIONAL CENTRE FOR THEORETICAL PHYSICS
34100 TRIESTE (ITALY) - P.O.B. 586 - MIRAMARE - STRADA COSTIERA 11 - TELEPHONE: 2240-1
CABLE: CENTRATOM - TELEX 460392 - I

H4.SMR/193 - 51

"COLLOQUE INTERNATIONAL SUR LA SCIENCE DES MATERIAUX POUR L'ENERGIE".
(26 août - 11 septembre 1986).

"SPECTRALLY SELECTIVE SURFACES FOR HEATING AND COOLING APPLICATIONS".

C.G. Granqvist
Chalmers University
Gothenburg, Sweden

SPECTRALLY SELECTIVE SURFACES
FOR HEATING AND COOLING APPLICATIONS

C.G. Granqvist
Physics Department, Chalmers University of Technology,
S-41296 Gothenburg, Sweden

Lecture notes covering the contents of
"Materiaux pour refroidissement radiatif"
and
"Materiaux à sélectivité radiative"
given during Colloque International sur la Science des
Materiaux pour l'Energie,
Trieste 26 Aug. - 9 Sept., 1986.

CONTENTS

CONTENTS

1. INTRODUCTION

Heat transfer occurs via radiation, conduction and convection. When the radiative exchange is significant - which holds true for many important applications - one can achieve energy efficiency by exploiting surfaces with spectral selectivity. This term is taken to imply that the radiative properties (i.e., the absorptance A, emittance E, reflectance R, and transmittance T) are qualitatively different within different parts of the electromagnetic spectrum. Spectral selectivity is often obtained by use of coatings onto substrates which are either transparent or opaque metallic.

The optical properties are connected to one another at each wavelength λ by the general relations

$$A(\lambda) + R(\lambda) + T(\lambda) = 1, \qquad (1)$$

$$E(\lambda) = A(\lambda). \qquad (2)$$

Both relations follow from energy conservation. Equation (2), known as Kirchhoff's law, states that at a given wavelength the absorptance is equal to the emittance for matter in thermodynamical equilibrium.

In the lectures summarized on the following pages, we consider three important applications of selective coatings. These are for

- selective transmission to achieve energy efficient windows;
- selective absorption of solar energy in order to produce useful heat;
- radiative cooling by selective infrared emission towards the clear sky.

Section 2 contains some basic material which must be covered before we can turn to the selective surfaces. It treats thin film optics, models for dielectric functions of uniform and non-uniform materials, and techniques to evaluate dielectric functions from optical measurements. Section 3 introduces spectral selectivity for heating and cooling purposes by presenting the radiative properties pertinent to our ambience and giving formulas for computing suitably integrated optical quantities. Section 4 is devoted to window coatings of different types and covers the spectral selectivity demanded for hot and cold climates, a review over coatings for "solar control" and for obtaining low thermal emittance, a case study of the optical properties of ion-plated Au films, another case study of e-beam evaporated In_2O_3:Sn films, and a survey over optical switching coatings of electrochromic and thermochromic type. The case studies are not as restrictive as one may first believe but illustrate the salient features of coatings based on noble metal films and on heavily doped oxide semiconductor films. Section 5 takes up surfaces for selective absorption of solar energy. Such surfaces are needed in efficient solar collectors. We cover the required spectral selectivity, give a review of coatings, and present a case study on coevaporated Co-Al_2O_3 composite films. Section 6, finally, dwells on materials for radiative cooling to low temperatures. The resource for radiative cooling under a clear sky, materials with infrared-selective emission, and infrared-transparent convection shields are discussed. The reference list at the end of these notes contains books, review articles and - to a limited extent - original scientific papers of particular relevance. General reviews over selective surfaces for heating and cooling are given in Refs. 1-6.

2. NOTES ON THE OPTICAL PROPERTIES OF MATERIALS

2.1 Basic thin film optics

We consider light incident towards the boundary between two media denoted i and j. The angle to the surface normal is θ_i, as indicated in Fig. 1. The media are characterized by their complex dielectric functions ε_i and ε_j. Part of the light is reflected at the boundary (r^{ij}) and part is transmitted (t^{ij}) through the boundary. We distinguish between light with s-polarisation (E vectors normal to the plane spanned by the incident, reflected and transmitted beams) and with p-polarisation (H vectors normal to the same plane). From Maxwell's equations, one can now obtain the well known Fresnel's relations for the reflected field amplitudes.

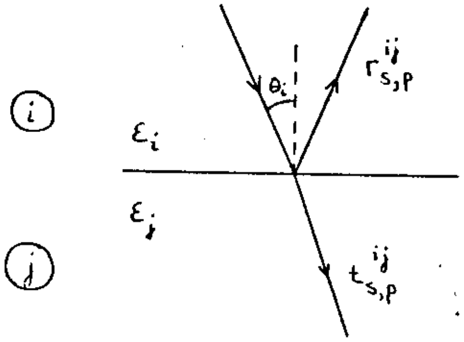

Figure 1. Definition of symbols entering Fresnel's relations.

$$r_s^{ij} = \frac{(\varepsilon_i)^{1/2}\cos\theta_i - (\varepsilon_j - \varepsilon_i\sin^2\theta_i)^{1/2}}{(\varepsilon_i)^{1/2}\cos\theta_i + (\varepsilon_j - \varepsilon_i\sin^2\theta_i)^{1/2}}, \qquad (3)$$

$$r_p^{ij} = \frac{(\varepsilon_i)^{1/2}(\varepsilon_j - \varepsilon_i\sin^2\theta_i)^{1/2} - \varepsilon_j\cos\theta_i}{(\varepsilon_i)^{1/2}(\varepsilon_j - \varepsilon_i\sin^2\theta_i)^{1/2} + \varepsilon_j\cos\theta_i}, \qquad (4)$$

$$t_s^{ij} = \frac{2(\varepsilon_i)^{1/2}\cos\theta_i}{(\varepsilon_i)^{1/2}\cos\theta_i + (\varepsilon_j - \varepsilon_i\sin^2\theta_i)^{1/2}}, \qquad (5)$$

$$t_p^{ij} = \frac{2(\varepsilon_i\varepsilon_j)^{1/2}\cos\theta_i}{(\varepsilon_i)^{1/2}(\varepsilon_j - \varepsilon_i\sin^2\theta_i)^{1/2} + \varepsilon_j\cos\theta_i}. \qquad (6)$$

Fresnel's relations can be used to discuss the optical properties of a thin film on a substrate. We consider the geometry specified in Fig. 2 and let (2) denote the film (of thickness d) and (3) the substrate. A medium (1) surrounds the coated substrate. Further we let (f) signify light incident from the frontside and (b) signify light incident from the backside.

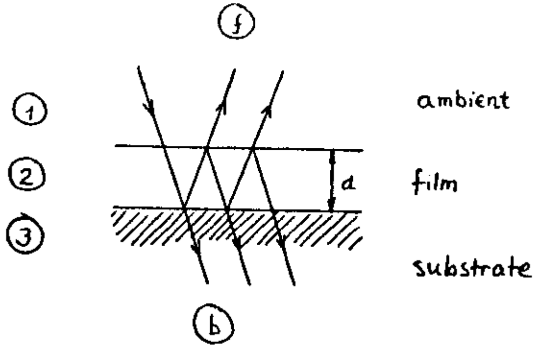

Figure 2. Geometry for discussing the optics of a thin film on a substrate.

Equations (3) - (6) yield expressions for r^{12}, r^{23}, t^{12}, t^{21}, t^{23}, t^{32}, r^{31} and t^{31}. Neglecting the effect of the backside of the substrate, we obtain the reflectance and transmittance amplitudes for the film, r_2 and t_2, by

$$r^f_{2s} = \frac{r^{12}_s + r^{23}_s e^{2i\delta}}{1 + r^{12}_s r^{23}_s e^{2i\delta}}\,, \tag{7}$$

$$t^f_{2s} = \frac{t^{12}_s t^{23}_s e^{i\delta}}{1 + r^{12}_s r^{23}_s e^{2i\delta}}. \tag{8}$$

Relations of the same form are easily found for r^b_{2s}, t^b_{2s}, $r^{f,b}_{2p}$, $t^{f,b}_{2p}$ as well. In Eqs. (7) and (8), δ is the phase change of the light beam upon traversing the film. Specifically

$$\delta = \frac{2\pi}{\lambda}(\varepsilon - \sin^2\theta_1)^{1/2}d. \tag{9}$$

The measurable optical quantities are light intensities. These are the squares of the absolute values of r^f_{2s} etc., denoted by capital letters, i.e. for example R^f_{2s}.

If the substrate is metallic, then the transmittance is zero and only the reflectance has to be considered. Thus the reflectance for s-polarised light is obtained simply by squaring the absolute value of Eq. (7), and the reflectance for p-polarised light is obtained in the same manner from an expression analogous to Eq. (7).

If the substrate is transparent, a more complicated situation exists, and multiple reflections in the substrate must be taken into account. They are incoherent for large substrate thicknesses and must be included through addition of the intensities of the multiply reflected beams. The final expressions for the reflectance and the transmittance are,

$$R_s = R^f_{2s} + \frac{T^f_{2s}T^b_{2s}R_{3s}}{1 - R^b_{2s}R_{3s}}\,, \tag{10}$$

$$T_S = \frac{T^f_{2s}T_{3s}}{1 - R^b_{2s}R_{3s}}, \tag{11}$$

where $T_{3s,p} = |r^{31}_{s,p}|^2$ and $T_{3s,p} = |t^{31}_{s,p}|^2$. Analogous relations are obtained for the p-components.

Detailed descriptions of thin film optics may be found in the books by Heavens (Ref.7) and by Born and Wolf (Ref. 8). Among many other things, these books discuss how to treat multiple layer films through matrix techniques.

2.2 Dielectric functions of uniform model materials.

The optical properties of a material are conveniently discussed in terms of a complex frequency-dependent dielectric function $\varepsilon(\omega) = \varepsilon_1(\omega)+i\varepsilon_2(\omega)$. Alternatively, one may use a complex refractive index $N \equiv n + ik = \varepsilon^{1/2}$. In the latter notation, n and k are known as the optical constants of the material.

In many cases one can regard ε as a sum of individual contributions originating from different elementary excitations (cf, for example, the book by Mahan (Ref.9)). In terms of susceptibilities $\chi^i \equiv \chi_1^i + i\chi_2^i$, (in SI units) one can write

$$\varepsilon = 1 + \chi^{VE} + \chi^{PH} + \chi^{FC}, \qquad (12)$$

where VE = valence electrons, PH = phonons, and FC = free carriers (usually electrons). The various susceptibilities can easily be distinguished if their resonances fall in well separated wavelength regions. For a particular χ^i, the contribution far from its resonance is real and constant.

Figure 3 gives a schematic representation of the χs^i. The real and imaginary parts are consistent with the Kramers-Kronig relations. For χ^{VE} and χ^{PH}, one can often represent the susceptibilities by a sum of damped Lorentz oscillators, i.e. by expressions of the kind

$$\chi^{Lorentz} = \frac{\Omega^2}{\omega_L{}^2 - \omega^2 - i\omega\Gamma} , \qquad (13)$$

where Ω is the oscillator strength, ω_L is the resonance frequency and Γ represents the width of the resonance peak. For most good metals, χ^{VE} is resonant in the ultraviolet, while χ^{PH} is resonant in the thermal infrared. For χ^{FC}, one can make use of the Drude theory, at least for a first-order description. The susceptibility can be written

$$\chi^{Drude} = - \frac{\omega_p{}^2}{\omega^2 + i\omega\gamma} , \qquad (14)$$

where ω_p is the plasma frequency and γ represents the width of the resonance. More elaborate free-electron theories are required for quantitative assessments. It is seen that χ^{Drude} can be obtained by setting $\omega_L = 0$ in $\chi^{Lorentz}$. Below $\hbar\omega_p$, χ_1^{FC} becomes strongly negative while χ_2^{FC} becomes strongly positive, as apparent from Fig. 3. The location of $\hbar\omega_p$ depends on the free electron density. For a metal, $\hbar\omega_p$ is normally in the ultraviolet. For a doped semiconductor, $\hbar\omega_p$ can be in the infrared. In a metal, χ^{PH} is usually not apparent owing to the dominating influence of χ^{FC}. The lowest part of Fig. 3 illustrates the ensuing performance of ε for a heavily doped semiconductor.

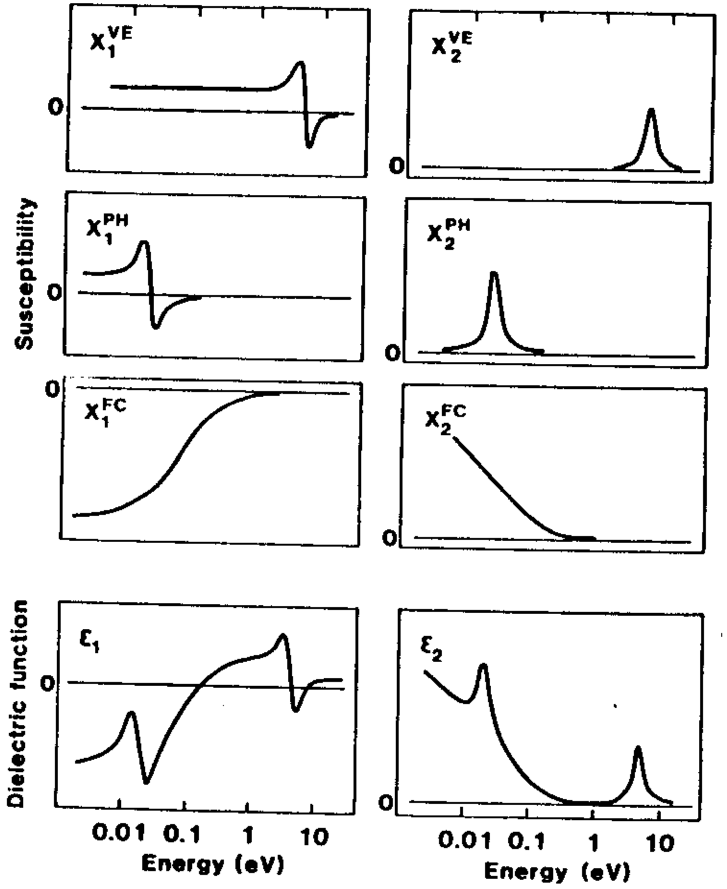

Figure 3. Contributions to the dielectric function from susceptibilities due to valence electrons, phonons, and free carriers.

2.3 Dielectric functions for non-uniform model materials

Surface coatings of interest for heating and cooling purposes, as well as for other applications, are often non-uniform on a scale which is much smaller than the wavelengths of concern. Frequently, the coatings comprise a mixture of metallic and insulating components. Under these conditions, the optical performance of the coating is governed by a spatial average of the properties of the two components. The averaging, which is far from trivial for non-dilute composites, is expressed in terms of an effective-medium theory (EMT), which yields an effective dielectric function $\bar{\varepsilon}$.

EMTs are of importance both for basic scientific reasons and also because they permit modeling and optimization of the optical performance of coatings by use of a computer. Many EMTs have been formulated and investigated recently. Much of this work has been motivated by its potential interest for efficient solar energy utilization. Reviews are given in Refs. 10-14.

Figure 4 serves as a background for the formulation of different EMTs. The averaging needed in the derivation of $\bar{\varepsilon}$ depends crucially on the specific microgeometry of the composite, and parts (a) and (b) show two structures which are characteristic for many practically occurring two-component composites. In order to formulate the EMTs, we want to single out the essential feature of the structure; thus we need simplifying assumptions which do not leave out the basic physics. This is done by the introduction of random unit cells (RUCs), as shown in Figs. 4 (c) and (d). The separed-grain structure is represented by a sphere of "A" surrounded by a concentric shell of "B", and the aggregate structure is represented by a sphere having a probability f_A of being "A" and $1-f_A$ of being "B".

A basic definition of an effective medium is that the RUC - embedded in the effective medium - should not be detectable in an experiment using radiation confined to a specified wavelength range. Thus the extinction of the RUC should be the same as if it were replaced by a sphere whose dielectric function is $\bar{\varepsilon}$. An optical theorem for absorbing media states that

$$C_{ext} = 4\pi \ \mathrm{Re}\left[S(0)/k^2\right], \tag{15}$$

$$k = 2\pi\bar{\varepsilon}^{\,1/2}/\lambda, \tag{16}$$

where C_{ext} is the extinction of the RUC compared with that of the surrounding material and S(0) is the scattering amplitude in the forward direction. Requiring now that $C_{ext} = 0$ yields

$$S(0) = 0, \tag{17}$$

which states the fundamental property of an effective medium.

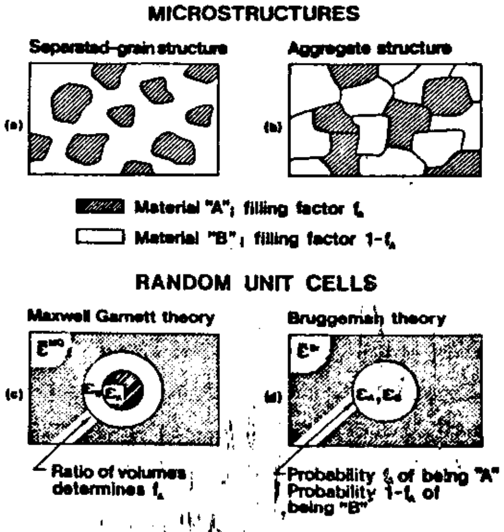

Figure 4. Microstructures and random unit cells for two types of composite materials.

The RUC of the separated-grain structure is a coated sphere (cs) which yields[15-17]

$$S^{cs}(0) = i(kb)^3\,\frac{(\varepsilon_B - \bar{\varepsilon})(\varepsilon_A + 2\varepsilon_B) + f_A(2\varepsilon_B + \bar{\varepsilon})(\varepsilon_A - \varepsilon_B)}{(\varepsilon_B + 2\bar{\varepsilon})(\varepsilon_A + 2\varepsilon_B) + f_A(2\varepsilon_B - 2\bar{\varepsilon})(\varepsilon_A - \varepsilon_B)} + O\left[(kb)^5\right]. \tag{18}$$

The "filling factor" is given by $f_A = (a/b)^3$, where a(b) denotes the radius of the inner (outer) sphere. For small particles, we set the leading term in $S^{cs}(0)$ equal to zero and obtain (with $\varepsilon \equiv \varepsilon^{MG}$)

$$\frac{\bar{\varepsilon}^{MG} - \varepsilon_B}{\bar{\varepsilon}^{MG} + 2\varepsilon_B} = f_A\,\frac{\varepsilon_A - \varepsilon_B}{\varepsilon_A + 2\varepsilon_B}\,, \tag{19}$$

which is the well known expression for the effective dielectric function of the Maxwell Garnett (MG) theory.[18]

The RUC of the aggregate structure is a sphere (s) with[15-17]

$$S^{s}(0) = i(kb)^3\,\frac{\varepsilon - \bar{\varepsilon}}{\varepsilon + 2\bar{\varepsilon}} + O\left[(kb)^5\right], \tag{20}$$

where ε is either ε_A or ε_B. In the small size limit we obtain (with $\bar{\varepsilon} \equiv \bar{\varepsilon}^{Br}$)

$$f_A\,\frac{\varepsilon_A - \bar{\varepsilon}^{Br}}{\varepsilon_A + 2\bar{\varepsilon}^{Br}} + (1 - f_A)\,\frac{\varepsilon_B - \bar{\varepsilon}^{Br}}{\varepsilon_A + 2\bar{\varepsilon}^{Br}} = 0. \tag{21}$$

This equation was first given by Bruggeman (Br).[19]

It is possible to extend the EMTs to non-spherical particles and also to set limits on the permissible particle diameters. These and other aspects are treated in Ref. 20. Finally, we note that there have appeared certain general results (Bergman-Milton bounds) for $\bar{\varepsilon}$ which hold irrespective of the detailed microgeometry.[21,22]

2.4 Evaluation of dielectric functions from optical measurements

The extraction of optical constants of thin films from various types of optical measurements is a field of widespread interest, and a large number of schemes using thin films for the determination of optical constants have consequently been devised in the literature. The current interest in coatings for energy efficiency has further created a new demand for routine techniques of determining the optical constants of materials in the visible and infrared wavelength regions. Such techniques should be experimentally straightforward, compatible with conventional equipment, and applicable in a wide wavelength range.

The most commonly used technique to determine practically the optical constants n and k of materials involves measuring the normal incidence transmission T and the near normal incidence reflection R of a thin film on a transparent substrate. We refer to this technique as the (T,R) method. It derives its popularity mainly from the experimental simplicity. No angular adjustments, polarizers, or others special equipment are needed, unintentional polarization effects in the optical system do not enter, and the sample preparation is straightforward. An alternative technique, known as the (T,R_m) method combines normal incidence transmission with near-normal reflection R_m against a metallized part of the substrate. The latter technique is particularly useful for absorbing materials.

The (T,R)- and (T,R_m) methods have their specific pros and cons, which may be conveniently illustrated from contour maps. These show computed curves for constant R,T and R_m in the (n,k) plane. Figure 5 shows a contour map for T(n,k) and R(n,k) at wavelength λ for a thin film of thickness d, so that $d/\lambda = 0.1$. The film is backed by a transparent substrate with refractive index $n_s = 1.5$. One notes that the transmission contours constitute a very regular grid in the (n,k) plane with the contours running virtually parallel to each other over a large region. The transmission value is evidently determined almost solely by the imaginary part of the refractive index whereas the dependence of the real part of the refractive index is very weak. To obtain an accurate technique for determining n and k, the transmission data should be combined with an experiment with a regular grid of contours oriented approximately perpendicularly to the transmission grid. The accuracy of the determined optical constants is governed by two factors, namely, by the spacing of the grids and by their angle of intersection ψ. A small spacing and perpendicular orientation yields the highest accuracy. For other orientations the inaccuracy is proportional to 1/cos ψ. Clearly the (T,R) combination is far from ideal. As shown in Fig. 5, the R contours make a suitably oriented grid in very limited regions of the (n,k) plane. Notably only for large k and small n ($k > 1$, $n < 1$) and for very small k values near the n axis do the contours intersect under a suitable angle. For almost any point in the (n,k) plane at which $n > k$, the angle of intersection is quite small, leading to increased errors of the (T,R) method. Furthermore, in a region close to the line $n = k + 1$, the transmission and reflection contours run parallel to each other and as a result even a minor experimental error in this region leads to gross errors in the extracted optical constants, particularly in the real part. A further problem of the (T,R) method is the fact that several solutions (n,k) exist to each set (T,R). This multivaluedness, which is an inherent property of any technique using two intensity measurements, produces a problem in the (T,R) case in regions near the contour tangency points, which are branch points between different solutions. A minor experimental error in this region can cause a branching from one solution (n_1,k_1) to another solution (n_2,k_2) which is physically incorrect.

Figure 6 gives a contour plot for the (T,R_m) case. Contours of constant transmission T of a thin film $(d/\lambda = 0.1)$ on a transparent substrate $(n_s = 1.5)$ are combined with contours of the thin film reflection R_m on a metallic substrate. The optical constants of the substrate metal, $n_m + ik_m$, were arbitrarily set to $n_m = 20$, $k_m = 70$, which is typical of aluminium in the mid-infrared. The exact choice of optical constant plays a very subordinate role for this contour plot. The (T,R_m) contour map evidently differs from the (T,R) map in several important ways. Particularly noteworthy is the fact that the R_m contours form a regular grid oriented almost perpendicularly to the transmission contours in a large region of the (n,k) plane

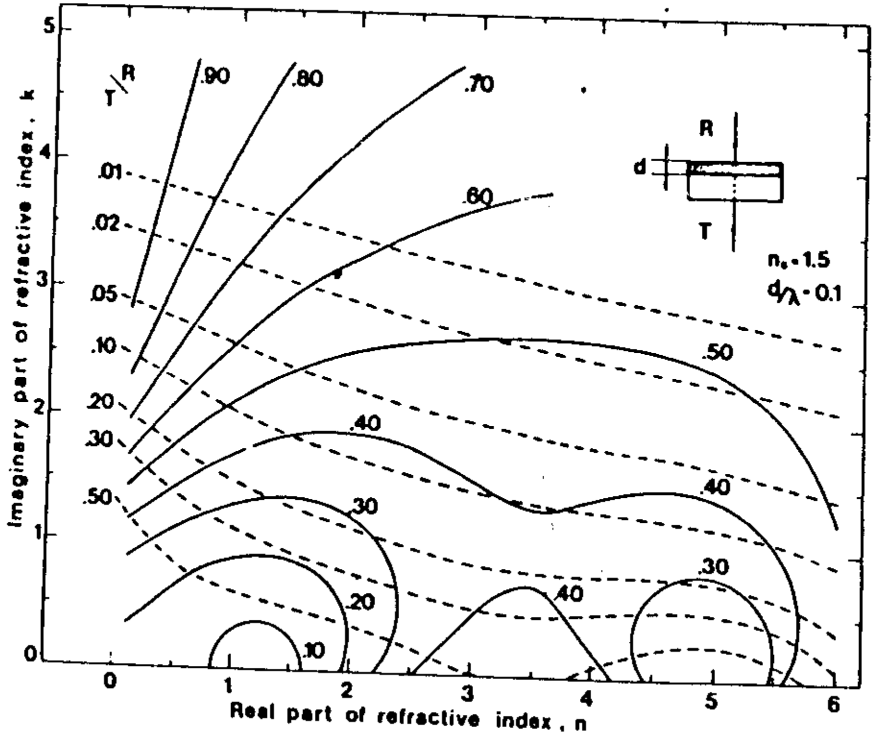

Figure 5. *Plot of the contours of constant normal transmission T and reflection R of a thin film, $d/\lambda = 0.1$, on a transparent substrate, $n_s = 1.5$.*

(for $n \lesssim 2.4$). This means that the (T,R_m) combination makes an excellent technique for the determination of thin film optical constants in this part of the (n,k) plane. It is interesting to note that this good region of the (T,R_m) technique includes the inherently troublesome region of the (T,R) technique. The pole structure apparent in Fig. 6 can be moved by having a different thickness of the film. This feature extends the applicability of the (T,R_m) technique. A more detailed discussion of the (T,R) and (T,R_m) methods, including error analyses, can be found in Ref. 23.

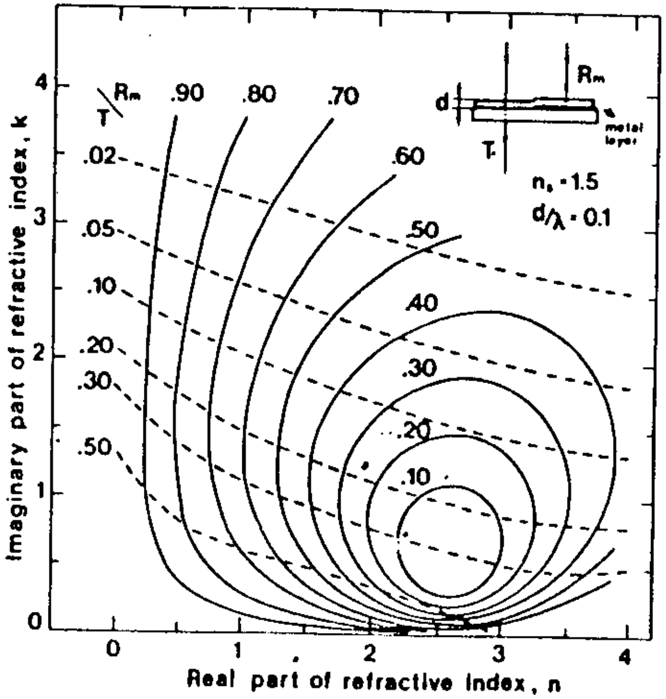

Figure 6. *Plot of the contours of constant normal transmission T and reflection R_m of a thin film, $d/\lambda = 0.1$, on a partly metallized substrate. Thin film refractive index $n + ik$, transparent substrate index $n_s = 1.5$ and metal substrate index $20 + i70$.*

The above mentioned optical techniques for evaluating ε_1 and ε_2 or n and k are by no means the only ones. A class of techniques is based on measurements of polarimetric ratios. It has been shown to yield very high precision, mainly in the visible wavelength range. It relies however for its accuracy on excellent wide range polarizers and a very well collimated beam. These are demands that are not easily met, particularly in the infrared. Specialized equipment (ellipsometers) are also needed to take full advantage of the technique. Experimental methods, based on a single optical measurement of, e.g., transmission or reflection and subsequent use of the causality relations (Kramers-Kronig) of the optical constants to obtain n and k, have the drawback that experimental data over an extremely wide wavelength range are needed; in principle, all the way from zero to infinite wavelength. A very direct approach utilizes Fourier transform interferometers, which measure amplitude as well as phase in a transmission or reflection experiment. This method has so far been restricted mainly to the (far) infrared region and also demands sophisticated and specialized equipment. An exhaustive survey over techniques to determine ε or n and k is given in Ref. 24.

3. SPECTRAL SELECTIVITY

3.1 Ambient radiative properties

Spectral selectivity, as a means to achieve energy efficiency, rests on the radiative properties of our ambience. These are illustrated in Fig. 7 with a common logarithmic wavelength scale on the abscissa. Part (a) depicts blackbody spectra for four temperatures of practical interest. The vertical scale gives power per unit area and wavelength increment. The curves appear bell-shaped. Practically no energy is emitted for wavelength shorter than

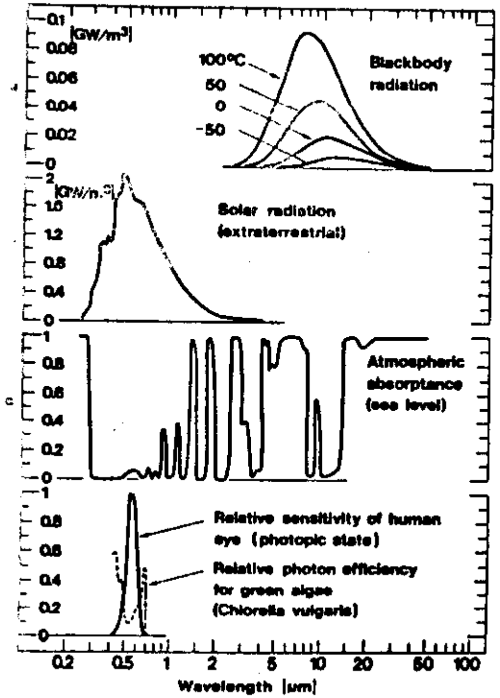

Figure 7. *Spectra for (a) blackbody radiation pertaining to four temperatures, (b) solar irradiation outside the earth's atmosphere (c) typical absorptance across the full atmospheric envelope, (d) relative sensitivity of the human eye and relative photon efficiency of leaves in living plants.*

2 µm. Blackbody spectra pertaining to room temperature are peaked at ~10 µm. The thermal radiation from a real body is obtained by multiplying the blackbody radiation by a numerical factor - the emittance - which is less than unity. In general, the emittance is wavelength dependent.

Figure 7 (b) shows the spectrum for solar radiation incident on the atmospheric envelope. The curve agrees rather well with a blackbody spectrum defined by the sun's surface temperature (~ 6000 ^{0}C). We observe that the solar spectrum is confined to the 0.25 - 3-µm interval, so that there is almost no overlap with the thermal spectra in part (a). Hence one can have surfaces whose properties are entirely different with regard to thermal and solar radiation, as we return to for window coatings in Section 4 and for solar collector surfaces in Section 5.

The applications of present interest take place at ground level, and hence it is important to consider the role of the atmosphere. Figure 7 (c) shows typical absorptance vertically across the atmospheric envelope. The pronounced peaks are due to molecular absorption in water vapour, carbon dioxide, and ozone. It is seen that most of the solar radiation can be transmitted through the air. In contrast, the thermal radiation from an upwards facing surface is absorbed to a large extent except at 8 to 13 µm where the absorptance is weak (provided that the atmospheric humidity is not too large). The thermal radiation can be large in the 8-13-µm interval, and hence we conclude that a non-negligible part of the emitted energy can go straight through the atmosphere. This phenomenon constitutes the basis for radiative cooling, which is further treated in Section 6.

Figure 7 (d) presents two biological constraints which are important for some applications. The solid curve shows that human eye is sensitive only in the 0.4-0.7 µm range. Hence a large part of the solar energy comes as infrared radiation, which is an important fact for window coatings as will

be discussed in Section 4. The dashed curve shows that photosynthesis in green plants uses radiation with wavelengths shorter than 0.7 µm.

3.2 Integrated optical properties

For assessing the performance of surfaces with regard to energy efficiency, we must know one or several suitably averaged optical properties. The integration could be over the eye's sensitivity curve (to get the luminous performance), over a typical solar spectrum, over a blackbody spectrum to get the thermal performance, or over the atmospheric irradiance spectrum to find the radiative cooling performance. Luminous, solar and thermal quantities are discussed here, whereas the treatment of radiative cooling is postponed to Section 6. Colour specifications also uses integrated optical quantities.

Integrated luminous (lum), solar (sol), and thermal (therm) quantities are conveniently obtained from the relation

$$X_\gamma = \int d\lambda \phi_\gamma(\lambda) X(\lambda) / \int d\lambda \phi_\gamma(\lambda). \qquad (22)$$

Depending on which quantity we want to compute, we set ϕ_γ equal to ϕ_{lum}, ϕ_{sol} or ϕ_{therm}. For the function ϕ_{lum} it is proper to use the standard luminous efficiency function for photopic vision as specified by CIE (Ref. 25). For ϕ_{sol} one could use tabulated spectra appropriate to a certain air mass (AM) and turbidity (Ref. 26). For example one could use AM0 (extraterrestrial conditions), AM1 (sun at zenith), AM2 (sun at 30° above the horizon) etc. For ϕ_{therm}, the weighting function can be written

$$\phi_{therm} = c_1 \lambda^{-5} \left[\exp(c_2/\lambda\tau) - 1 \right]^{-1} \qquad (23)$$

with $c_1 = 3.7418 \times 10^{-16} \left[Wm^2 \right]$, $c_2 = 1.4388 \times 10^{-2} \left[mK \right]$, and τ signifying temperature. X in Eq. (22) denotes the spectral property; for example normal transmittance, normal reflectance, or hemispherical emittance E. The emittance can be obtained from

$$E(\lambda) = 1 - T_h(\lambda) - R_h(\lambda), \qquad (24)$$

where T_h is the hemispherical transmittance given by

$$T_h(\lambda) = \frac{1}{2} \int_0^{\pi/2} d(\sin^2\theta) \left[T_s(\theta,\lambda) + T_p(\theta,\lambda) \right], \qquad (25)$$

and an analogous relation holds for the hemispherical reflectance R_h. The subscripts s and [illegible] in Eq. (25) refer to different states of polarisation.

4. WINDOW COATINGS

4.2 The different types of spectral selectivity

We consider coatings which are transparent in at least part of the 0.3-100-µm range and discuss their applicability to energy efficient windows. This is a large subject, and in order to organize it we first consider coatings with *static properties*, i.e., coatings whose optical performance remains the same irrespective of external conditions. This group can be conveniently subdivided into coatings for "*solar control*" and for providing *low thermal emittance*. The second group of coatings, which is presently emerging as a self-contained research topic, have *dyanmic properties* and encompasses optical switching coatings of different types.

With the purpose of introducing the "solar control" coatings, we note that in a hot climate it is frequently the case that the solar energy which enters through a window and is absorbed in the room causes to much heat. Hence, there is a need for cooling to obtain a comfortable indoor temperature. Conventional air conditioning uses a lot of electrical energy, part of which can be saved by the use of proper window coatings. From the upper part of Fig. 8, which contains basically the same information as in Fig. 7, it is seen that only some of the solar radiation comes as visible light. It is clearly effective to have a coating which is transparent only for $0.4 < \lambda < 0.7$ µm while it is reflecting for $0.7 < \lambda < 3$ µm so that the infrared part of the solar radiation is excluded. This spectral profile is shown by the solid lines in the lower part of Fig. 8. The improvement caused by such a coating depends to some extent on the weather, but as a rule of thumb it is possible to decrease the solar heating by almost 50 % at negligible loss of visible transmittance.

We now turn to the coatings with low thermal emittance and note that in a cold climate a window is usually causing an undesired loss of energy. A large part of this loss is by thermal radiation to the ambience. It is clear

from the upper part of Fig. 8 that energy efficiency can be gained by coatings which are transparent for $0.3 < \lambda < 3$ µm, so that maximum use is made of the solar energy, while the emittance of thermal radiation is minimized. The required optical properties are hence high transmittance for $0.3 < \lambda < 3$ µm and high reflectance for $3 < \lambda < 100$ µm. This performance is indicated by the dashed lines in the lower part of Fig. 8. The advantage of low-emittance window coatings can be expressed in various ways: one is to state that the same thermal insulation can be obtained in a window with double glazing and one coating as in a window with triple glazing and no coating. The lower weight of the former alternative is an important benefit.

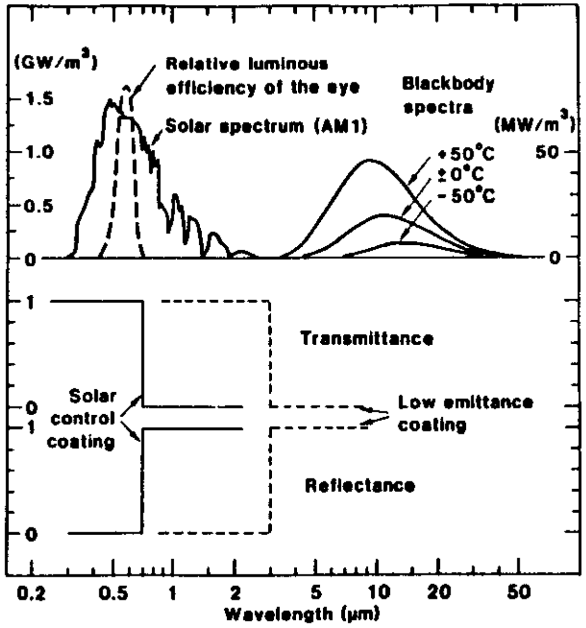

Figure 8. Upper part shows the luminous efficiency of the ligh-adapted eye, a typical solar spectrum for one air mass, and blackbody spectra corresponding to three temperatures. Lower part shows transmittance and reflectance for idealized window coatings designed for "solar control" (solid lines) and for low thermal emittance (dashed lines).

The previous two types of coatings are of great value for energy efficient windows. However, they have a fundamental limitation in their properties being static, which make them incapable of adjusting according to the variable demands on heating and lighting during the day or season. For example, it may be that a coating which has low thermal emittance, and is adequate during the winter in a midlatitude region, causes overheating during the summer. It is obvious that a "*smart window*" should exhibit radiative properties which can be automaticaly tuned in such a way that a suitable amount of solar energy or visible light is introduced. The pertinent coatings can be of different kinds:

photochromic (i.e., change their properties as a result of the irradiation); *thermochromic* (i.e., change their properties as a result of the temperature); and *electrochromic* (i.e., change their properties as a result of the strength and direction of an applied electric field). Here we focus mainly on the electrochromic ones. Research on switching coatings for energy efficient windows are presently being started in different parts of the world.

Reviews of window coatings with static properties are found in Refs. 27-43. Some work on electrochromic coatings is reviewed in Ref. 44. Useful information of window coatings is found also in Refs. 1-6.

4.2 Review of coatings with static properties

There exist several approaches to coatings which are transparent at short wavelengths and reflecting at long wavelengths. The simplest one is offered by very thin *metal films*. Best results are obtained for the free electron metals Cu, Ag and Au. Most other metals exhibit a pronounced undesirable interband absorption within the solar range.

The thickness of the coatings has to be above a certain threshold value, since otherwise they tend to be broken up in a two-dimensional array of discrete islands which do not exhibit metal-like properties. Figure 9, taken from Ref. 5, illustrates the salient properties of a growing metal film. Going from left to right, the figure presents growth stages, film structures, thickness scales and theoretical models for the optical properties. The growth stages are well known:[46,47] when metal vapour condenses onto a surface nuclei will be formed at certain sites; continued deposition makes the nuclei grow via surface diffusion and direct impingement; the metal islands thus formed undergo coalescence growth so that larger and

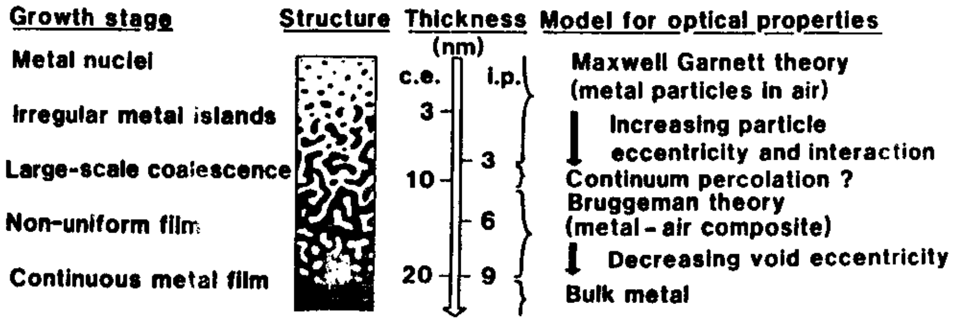

Figure 9. Survey of information on gold films coated onto glass by use of conventional evaporation (c.e.) and ion-plating (i.p.).

more irregular islands appear; the growing film then goes through large-scale coalescence so that a metallic network extends through the sample; subsequently the voids get smaller and more regular; and finally a uniform metal layer may be formed. The corresponding structures (with metal shown as black) are sketched. The thickness scales pertain to the deposition of gold onto glass by use of conventional evaporation as well as by ion-plating. One should note the compressed thickness scale valid for ion-plating. A similar compression - albeit perhaps not equally strong - is expected for sputtered films, since this deposition technique involves bombardment with energetic ions. This observation is important because magnetron sputtering is widely used today for the production of window coatings. Generally, the thickness scales are dependent on many parameters such as the deposited species, substrate material, substrate temperature, vacuum conditions, the presence of electric fields, etc. However, even if the thickness scales may display a varying degree of compression and expansion, it is expected that the growth stages are traversed in a certain order and hence that the optical performance varies with thickness in a definite way. The corresponding theoretical models for the optical properties are indicated in the right-hand part of Figure 9. The discontinuous metal film can be understood from the Maxwell Garnett theory (cf. Sec. 2.3), provided that particle shape and interaction - both of which become increasingly complicated with increasing thickness - are accounted for properly. Around large-scale coalescence, the film is characterized by an interpenetrating maze structure and we conjecture that effects of continuum percolation may be observable at optical frequencies. The non-uniform film can be understood to some degree from the Bruggeman theory (cf. Sec. 2.3) with due regard to void shapes. Finally, the continuous film can be understood to a considerable degree from the Drude theory (cf. Sec. 2.2). For a window coating to be practically useful, it should have a thickness well above the one required for large scale coalescence.

The optical properties of growing films, which were treated in principle in Fig. 9, are substantiated in Fig. 10. This figure is reproduced from a recent study[42] of selective transmission in conventionally evaporated films of Cu, Ag, Au, Cr, Fe, Co, Ni and Al. The shown data pertain to Ag coatings of different thicknesses onto glass. The thickest films (thickness 36 nm; curves denoted a) display an essentially bulk-like behaviour with high reflectance - and thus low transmittance - across the main part of the shown spectral range. For gradually thinner films, there is an increase in short-wavelength transmittance, while the reflectance for thermal radiation is not significantly affected. Thus there appears a gradual onset of selective transmission. For the thinnest film (thickness 6 nm; curves denoted e), a qualitatively different behaviour is encountered which is indicative of a discrete nature of the film. We return to the optical

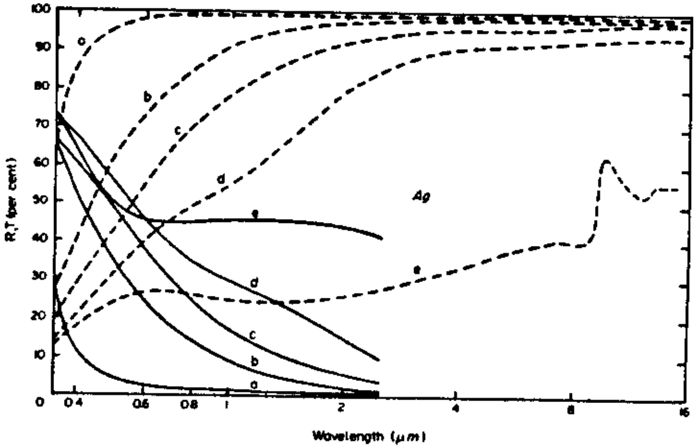

Figure 10. *Spectral transmittance (solid curves) and reflectance (dashed curves) of selectively transmitting silver films on glass substrates. The films have the following thicknesses: (a) 36 nm, (b) 16 nm, (c) 12 nm, (d) 9 nm, (e) 6 nm.*

properties of metal films in case study one reported on in Sec. 4.3.

The limited transmission in continuous noble-metal films is governed largely by reflection at the film boundaries rather than intrinsic absorption. Therefore it is possible to improve the transmittance by additional coating(s) which act so as to antireflect the metal. We are then led to consider dielectric/metal and dielectric/metal/dielectric multilayers. Dielectrics with high refractive indices (such as SnO_2, TiO_2, ZnO and ZnS) are useful for creating the desired induced transmission. By selecting proper thicknesses, one can optimize the coating either for solar control or for low thermal emittance. The optimization is conveniently done on a computer. Figure 11 reports on a high-performance selectively transmitting coating[29] suitable for solar control (according to the ideal property indicated by the dotted lines). The three-layer coating consists of titanium dioxide/silver/titanium dioxide, where each layer is 18 nm thick. The spectral transmittance and reflectance, shown by the solid curves, approach the ideal behaviour and, in particular, the visible transmittance is as large as about [illegible] %. The experimental data are in fair agreement with a computation (dashed curves) based on the known optical properties of the constituent materials. The ensuing differences are probably caused by a slightly non-homogeneous character of the silver layer.

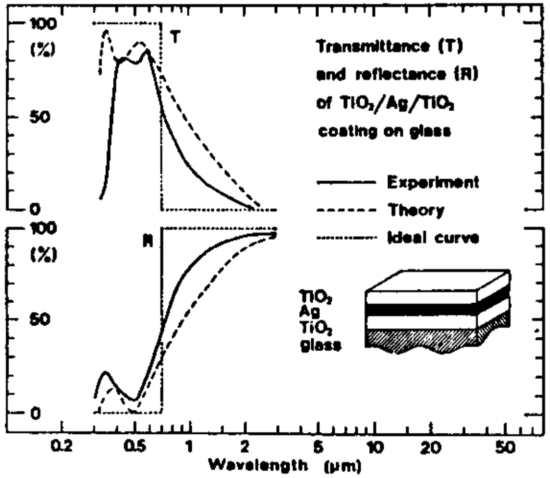

Figure 11. Spectral transmittance and reflectance of a TiO_2/Ag/TiO_2 coating on glass. Experimental and theoretical data are reported and compared with an ideal spectral profile. Inset depicts the coating structure.

Doped-semiconductor coatings offer another - principally superior - possibility. The energy gap must be sufficient to allow good transmission down to 0.3 µm and the structure must permit doping to a level so that the coating exhibits free-electron-like behaviour beyond a plasma wavelength of the order of a few µm. It is important that the doping does not introduce substantial absorption at wavelengths shorter than the plasma wavelength, and that the energy gap does not shift towards the visible range as a consequence of the doping. The useful materialsare oxide semiconductors based on Zn, Cd, In, Sn and combiantions of these. The required carrier densities can be achieved by non-stoichiometry (intrinsic doping) as well as by inclusion of foreign elements (extrinsic doping). Among the most widely studied materials we note SnO_2 doped by F or Sb, In_2O_3 doped via non-stoichiometry or by Sn, ZnO doped by Al, and Cd_2SnO_4.

The interesting oxide semiconductors have refractive indices of the order or 2, and hence the short wavelength transmittance is limited by reflection losses to an undesirable extent. One is then led to regard *dielectric/doped-semiconductor coatings*, for which the dielectric with low refractive index acts as an antireflecting layer. Figure 12 shows a specific case having particularly good performance: an Sn-doped In_2O_3 layer antireflected by MgF_2. It is found that the transmittance is high for short wavelengths (particularly in the visible) and that the reflectance is high for long wavelengths. These properties are rather good for a low-emittance window coating; they would have been even better if the onset of high reflectance were moved towards the infrared, as can easily be done by decreasing the Sn doping. We return to In_2O_3:Sn coatings in case study two in Sec. 4.4 below. We note that most low-refractive index coatings cannot be applied by high-rate sputtering, which is a drawback for practical production. An exception to this rule seems to be offered by certain novel metal-oxyfluoride coatings (Refs. 48, 49).

The final approach to selectively transmitting window coatings is to exploit some of the *new materials* which are appearing today. Interesting results have been found for TiN, LaB_6 and $AuAl_2$.

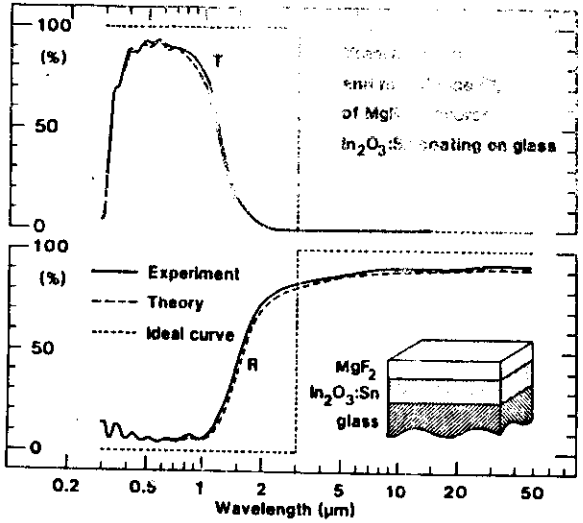

Figure 12. Spectral transmittance and reflectance of an MgF_2-coated In_2O_3:Sn film on glass. Experimental and theoretical data are reported and compared with an ideal spectral profile. Inset depicts the coating structure.

4.3 Case study one: Selective optical properties of ion-plated Au films (Ref. 45).

This first case study reports on the optical properties of thin gold films made by ion-plating and compares them with results obtained by conventional evaporation. Film thicknesses on either side of the magnitude required for microstructural uniformity are of interest. Several novel effects of potential importance for improved window coatings are identified and discussed in terms of theoretical models. There can be little doubt that these findings would apply equally well to films of Cu and Ag.

Figure 13 is a sketch of the film deposition system. Gold was evaporated onto unheated glass substrates and simultaneously onto grids for electron microscopy. The evaporation rate was maintained at a certain value r by use of a vibrating quartz microbalance connected to a microprocessor-based deposition controller which regulated the power delivered from the evaporation power supply. Most of the films were produced by ion-plating - i.e., by continuous bombardment of the growing film with energetic ions. The ion current, I, was recorded via a small probe in the ion beam.

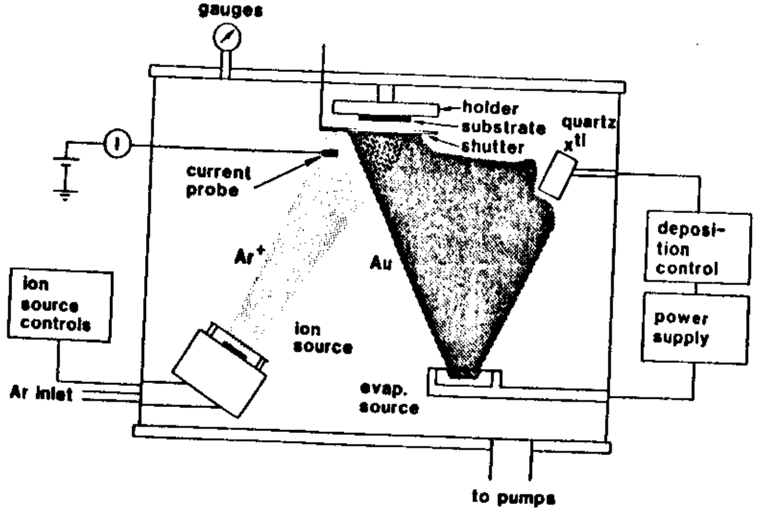

Figure 13. Schematic view of the ion-plating system and its process controls.

Ion-plating was performed as follows. After evacuation of the vacuum chamber an Ar flow was introduced so that the pressure became 10^{-4} Torr. The ion source was set to produce 500 eV Ar^+ ions with a certain flux $s(Ar^+)$, which was determined by measuring I. The gold flux s(Au) was inferred from r. Typical experimental parameters were $8 < I < 33$ A/cm^2 and $0.1 < r < 0.2$ nm/s. The flux ratio, defined by

$$g \equiv s(Ar^+)/s(Au), \qquad (26)$$

should be chosen properly in order to benefit from ion-beam-assisted film growth without having too much resputtering of deposited material. Empirically, we obtained good film properties with $g \approx 0.1$. Films with mass thicknesses in the range $4.5 < t < 18$ nm were produced.

The microsctructure of the coatings was investigated by transmission electron microscopy. Figure 14 shows a typical bright-field micrograph for a ion-plated (g=0.1) film with t = 5.5 nm. A characteristic network structure with an areal coverage > 75 % is observed. There is a striking similarity to the sketch in Fig. 9. Ion-plated films, made under favourable conditions,

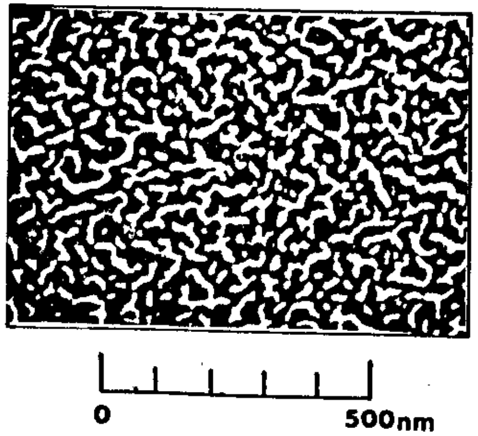

Figure 14. Transmission electron micrograph of a non-uniform ion-plated Au film.

had network configuration at $4 \lesssim t \lesssim 9$ nm and appeared uniform at $t \gtrsim 9$ nm. Without ion impingement (g = 0), we obtained network films at mass thicknesses as large as ~1[illegible] nm.

Figure 15 shows spectral tansmittance T and reflectance R in the visible and near-infrared. The left-hand part refers to ion-plated films obtained with g = 0.1. The thickest film (t ≈ 9 nm) displays an increase in R and a concomitant decrease in T for wavelengths $\lambda > 0.5\,\mu$m. This is characteristic for bulk-like Au, and we infer that the film is approaching a uniform structure. The lowering of T for $\lambda < 0.5\,\mu$m is caused by interband absorption. Thinner films are qualitatively different: for $6 < t < 9$ nm there are plateaus of T and R in the near-infrared, which are followed by a weak decrease in T

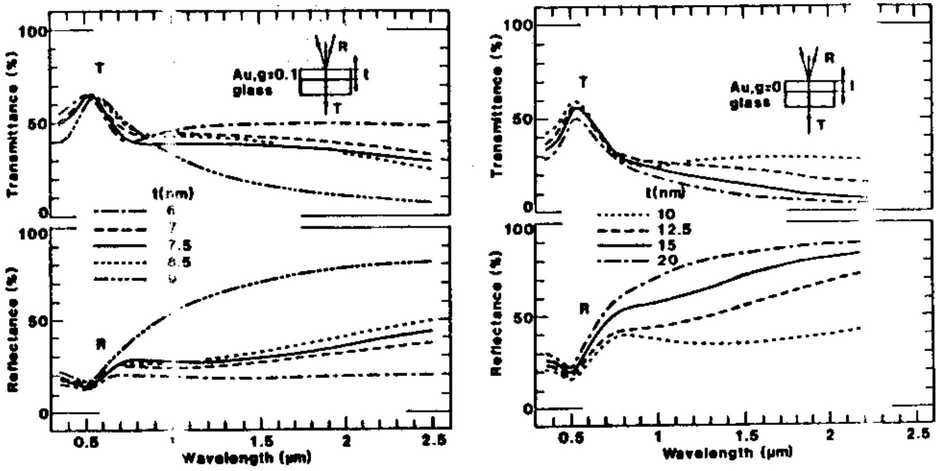

Figure 15. Spectral normal tansmittance and near-normal reflectance for thin Au films produced by ion-plating (left-hand part) and conventional evaporation (right-hand part) Data are shown for films with different mass thicknesses.

and increase in R at the longest wavelengths. It will be found below that the specific optical properties of films with $t < 9$ nm can be understood from considerations of non-uniform film structures. The right-hand part of Fig. 15 pertains to thicker films produced by conventional evaporation ($g = 0$). We note that near-infrared plateaus appear for $t \lesssim 15$ nm, which is well beyond the thickness where the ion-plated films seem to be entirely bulk-like. Curves resembling those in Fig. 15 have been reported also by Valkonen et al.[42] in the paper from which Fig. 10 was reproduced.

Figure 16 reports T_{sol} and R_{therm} versus t for Au films produced by ion-plating ($g = 0.1$) and by conventional evaporation ($g = 0$). These quantities were computed by use of the formulas given in Sec. 3.2 and $\tau = 300$ K.

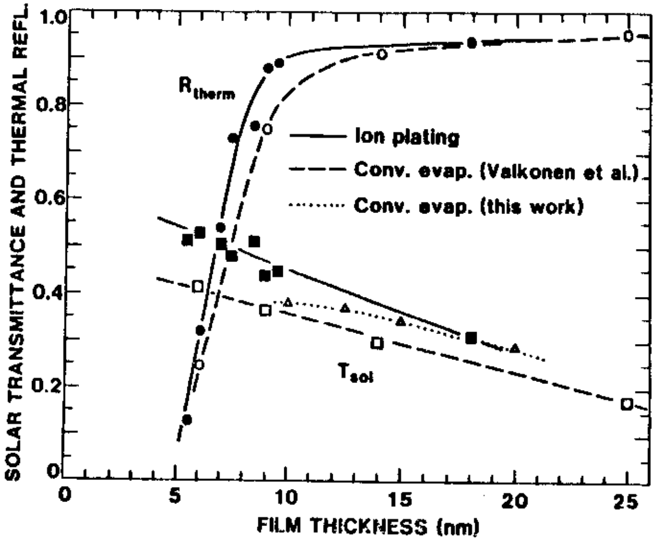

Figure 16. *Normal solar transmittance and near-normal thermal reflectance versus mass thickness for thin Au films produced by ion-plating (filled symbols) and by conventional evaporation (open symbols). Results from measurements by Valkonen et al. (Ref. 42) are included. Solid, dashed and dotted curves were drawn solely to guide the eye.*

The most important result concerns T_{sol}, which can be significantly enhanced as a result of the ion impingement. For example, one can combine $R_{therm} = 76$ % with $T_{sol} = 51$ % in an ion-plated film but only with $T_{sol} = 37$ % using conventional evaporation. Hence ion-plating can give significant gain in transmitted solar energy. Ion-plating also leads to some improvement in the thermal properties. All of the ion-plated films with $t < 9$ nm had $56 < T_{lum} < 58$ %. Large enhancements of T_{sol} and/or T_{lum} can be achieved by embedding the gold films between dielectric layers with high refractive indices, as we have already commented on.

We first analyze the thicker of the Au films - those with $t \gtrsim 9$ nm in the case of ion-plating. These films showed no evidence for non-uniformity, and it is meaningful to apply the Drude theory (Sec. 2.2) at $\lambda > 0.5$ μm. It was verified that, in fact, the Drude theory gives a very good representation of the extracted dielectric function for uniform Au films. The only feature worth further comment concerns the spectral dependence of the relaxation frequency γ (cf. Eq. 14) which is intriguingly strong. It was found that the experimental data were consistent with a relation

$$\gamma = \gamma^0 + \beta\omega^2, \tag{27}$$

where γ^0 and β are constants. An ω^2-dependence of the relaxation frequency has been reported before for metal films, but the present magnitude of β is considerably larger than the one found in earlier work on thicker films. Several mechanisms could yield a relation such as the one indicated in Eq. 27; we can mention electron-electron interaction, electron-phonon interaction, a two-carrier mechanism accounting for crystalline grains and disordered intergranular material, and surface electrodynamics. Recent work[50] showed convincingly that surface electrodynamics plays an important role. Our observation of enhanced βs in very thin ion-plated Au films is in accord with this view. The analysis also yielded a magnitude of γ^0 which is consistent with the film thickness and crystallite size.

We now turn to the analysis of the non-uniform films consisting of a mixture of gold and air-filled voids. Since the basic structural units cannot be taken as round, the Maxwell Garnett and Bruggeman EMTs must be generalized so as to account for appropriate values of the depolarisation factors. Specifically, we take the two-dimensional images of the films to comprise a metallic phase represented by circular units (with depolarisation factor L_m = 1/3, pertaining to spheres) and a dielectric phase represented by elliptical units (with depolarisation factors L_1 and L_2, so that $L_1 + L_2 = 1$). The generalization of Eq.(19) now reads

$$\frac{\bar{\varepsilon}^{MG} - \varepsilon_m}{\bar{\varepsilon}^{MG} + 2\,\varepsilon_m} = \frac{f}{6} \sum_{i=1}^{2} \frac{1 - \varepsilon_m}{\varepsilon_m + L_i(1-\varepsilon_m)} , \qquad (28)$$

and the generalization of Eq. (21) reads

$$\frac{f}{2} \sum_{i=1}^{2} \frac{1 + \bar{\varepsilon}^{Br}}{\bar{\varepsilon}^{Br} + L_i(1-\bar{\varepsilon}^{Br})} + (1-f)\,\frac{\varepsilon_m - \bar{\varepsilon}^{Br}}{\bar{\varepsilon}^{Br} + (\varepsilon_m - \bar{\varepsilon}^{Br})/3} = 0, \qquad (29)$$

where f is void fraction and ε_m refers to the dielectric function of gold modified by standard techniques[51] so as to encompass a short mean free path for the free electrons (set to 6.5 nm). It is then straight-forward to compute $\bar{\varepsilon}^{Br}$ and $\bar{\varepsilon}^{MG}$ versus λ, t, f, L_1 and L_m. Finally, we obtained T and R from Fresnel's equations (Sec. 2.1) and with the underlying substrate represented by the dielectric function for amorphous SiO_2 (Ref. 52).

Figure 17 shows spectral T and R for gold films characterized by different void fractions. We use t = 9 nm and the Bruggeman theory for circular structural units ($L_1 = L_2 = 1/2$). The dotted curves pertain to f = 0, i.e., to a uniform film. The calculated data are in good agreement with the measured results for the thickest films reported on Fig. 15. An increase of the void fraction is seen to have little effect on the luminous performance but to yield a considerable increase of T and decrease of R in the infrared. Figure 18 [illegible] several [illegible] results. It considers a gold film with t = 7.2 nm and f = 0.2. The solid curve refers to the Bruggeman theory for non-sperical voids (L_1 = 0.2). A comparison with the upper solid curve in Fig. 17 demonstrates that the departure from circular void shapes leads to a characteristic plateau across the 0.5 - 1 - µm range. Corresponding results based on the Maxwell Garnett theory do not produce a plateau but is otherwise in good agreement with the Bruggeman data, as seen

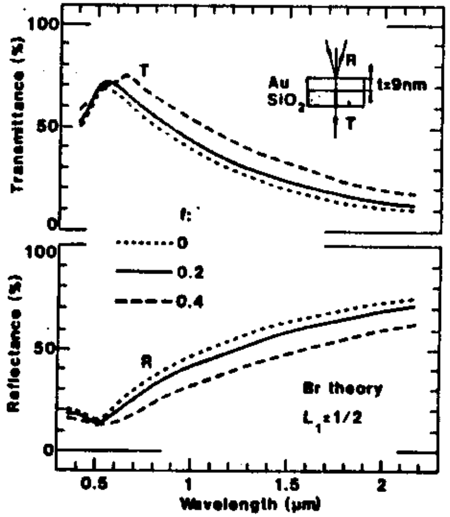

Figure 17. *Spectral normal transmittance and reflectance computed for a non-uniform Au film on SiO_2. The Bruggeman effective medium theory, appropriate to circular structural units, was used together with the shown values of mass thickness and void fraction.*

from the dashed curve in Fig. 18. Setting $L_m = 1/2$, as in the computation giving the dotted curve, does not lead to significant departures from the spectrum obtained with $L_m = 1/3$. The plateaus in the infrared transmittance are important since they affect the solar transmittance. The plateaus are further investigated in Fig. 19, where we vary L_1 from 0.5 (circle) to 0.1 for films with t = 9 nm and f = 0.2. The Bruggeman formalism is found that the plateaus become increasingly wide when L_1 is decreased (or the eccentricity of the elliptical voids is increased).

We now consider the computed spectra in some detail and discuss to what extent we can understand the spectrophotometric data. We focus on the conspicuous plateaus in the infrared spectra. They were clearly seen in the measured transmittance and were apparent also in computations based on the Bruggeman effective medium theory applied to non-spherical voids. Three specific points demand attention. First, we observed that the measured plateaus were widest in the thinnest film. Theoretically, this is to be expected since the most elongated voids occur closest to large scale coalescence

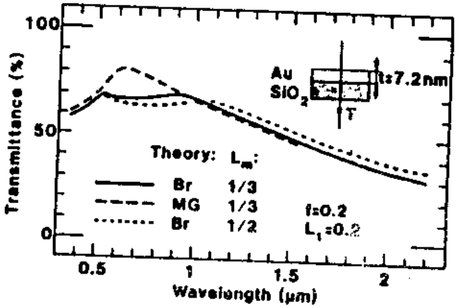

Figure 18. *Spectral normal transmittance computed for a non-uniform Au film on SiO_2. The Bruggeman and Maxwell Garnett effective medium theories were used together with the shown values of mass thickness, void fraction, and depolarisation factors for voids and metallic units.*

(or the percolation threshold). Second, the measured plateaus were less distinct than in the computations. This is also very reasonable when one remembers that a broad range of depolarisation factors is needed to characterize a real non-uniform film. Third, we observed that the transmittance maxima on the short-wavelength side of the plateaus were more prominent than expected from the Bruggeman theory. This is by no means unexpected, though, since the complex structure of the experimental samples makes one believe that features of both the Bruggeman and Maxwell Garnett theories are present. Indeed, combining the solid and dashed spectra in Fig. 18 makes the short-wavelength peak dominant. In conclusion, we find

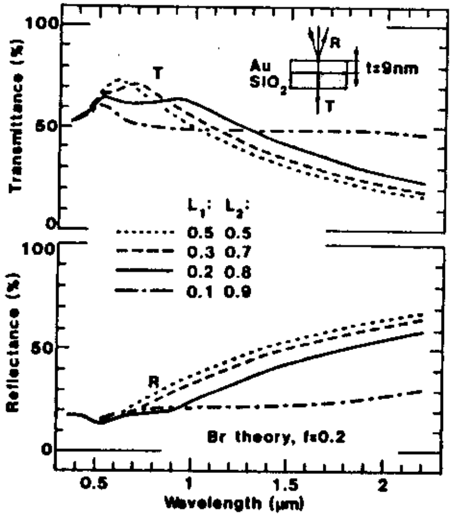

Figure 19. *Spectral normal transmittance and reflectance computed for a non-uniform Au film on SiO_2. The Bruggeman effective medium theory was used together with the shown values of mass thickness, void fraction, and depolarisation factors for the voids.*

that most features of the transmittance plateaus can be reconciled with an effective medium treatment based on the pertinent microstructure. This theory also explains the increased solar transmittance of properly produced non-uniform metal films.

4.4 Case study two: Selective optical properties of e-beam evaporated In_2O_3:Sn films (Refs. 53-59)

Coatings of In_2O_3:Sn (also known as indium-tin-oxide or ITO) have been investigated in depth during the last years. The theoretical understanding seems to be more advanced for this oxide semiconductor than for the other ones mentioned in Sec. 4.2. Hence we think it is worthwhileto present a detailed analysis of this particular material here.

In_2O_3:Sn coatings with selective optical properties can be produced by a variety of techniques including evaporation (resistive, e-beam; non-reactive, reactive) sputtering (diode, magnetron, ion-beam; planar, cylindrical; non-reactive, reactive), ion plating, chemical vapour deposition, spray pyrolysis, dipping etc. In the work to be discussed below we used reactive e-beam

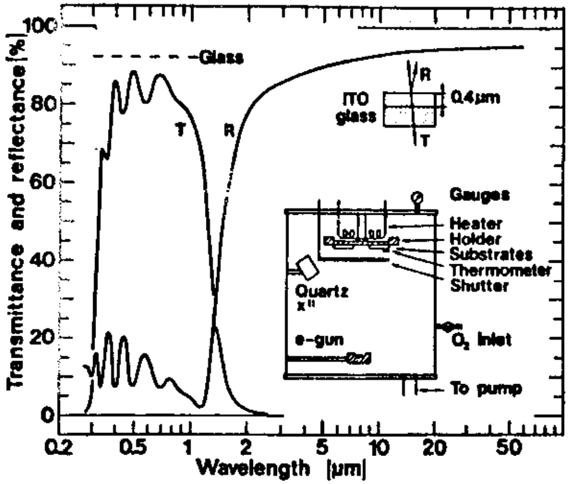

Figure 20. Spectral transmittance and reflectance of a 0.4 µm thick In_2O_3:Sn film on glass. Inset shows a sketch of the film deposition unit.

deposition of In_2O_3 + SnO_2 tablets onto heated substrates. This is a convenient technique for laboratory-type investigations, and it is also used for industrial production of In_2O_3:Sn coatings with high performance. The inset of Fig. 20 shows a sketch of the film production unit comprising a vacuum chamber with an e-beam source (whose input power is feed-back controlled from a vibrating quartz microbalance), a heated substrate holder, and facilities for controlled inlet of gases. In principle, this is the same deposition unit as the one shown in Fig. 13. We found that the best optical performance was obtained with substrate temperature ~ 300°C, constant evaporation rate in the 0.2-0.3 nm/s interval, and constant oxygen pressure in the $5\text{-}8 \times 10^{-4}$ Torr interval. Main part of Fig. 20 shows spectrophotometric measurements of transmittance and reflectance for a 0.4-μm-thick coating on glass. The spectral selectivity is similar to the one shown in Fig. 12, which is the expected result. The deposition parameters are rather crucial, which is true not only for evaporation but also for other techniques such as sputtering.[60,61] This is illustrated in Fig. 21, which shows the spectral absorptance across the visible range for 0.3-μm-thick In_2O_3:Sn films deposited at different temperatures. Only the film made at the highest temperature has very good performance. In our best films we have found an absorptance of only ~ 0.2 % at λ = 0.5 μm.

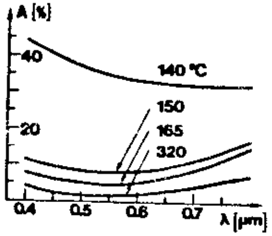

Figure 21. Spectral absorptance (A) for In_2O_3:Sn films (on glass) deposited at four different substrate temperatures.

In Fig. 20 it is seen that the visible transmittance exhibits pronounced peaks, which are indicative of optical interference. This will lead to a slight colouring of the coatings. Further, if small thickness variations exist across the coated surface - which may be hard to avoid for architectural coatings - it will show iridescence, which is definitely an unwanted effect for most applications. An improvement in the colour performance is achieved by antireflection coats. Comparing Figs. 12 and 20 it is evident that the MgF_2 layer significantly cuts down the iridescence. The actual MgF_2 thickness is 90 nm in this example. The luminous transmittance can be ~ 95 % (including the substrate) while the thermal emittance is ≤ 20 % for 0.3-μm-thick In_2O_3:Sn films antireflection coated with 90 nm of MgF_2.

Colour properties have not often received proper attention in scientific works on selectively transmitting window coatings. This is somewhat surprising, since colorimetric analysis is a well known subject treated in several books.[25,62-64] As an example of the quantitative results one can reach by colorimetric analysis, we present in Fig. 22 the x and y coordinates referred to the CIE 1931 standard colorimetric system and a daylight-type illuminant for normal transmission of light through glass coated with In_2O_3:Sn (thickness range 250 to 400 nm) and MgF_2 (thickness, t, being 0, 90, 95, 100, 105 nm). The data were computed by use of the dielectric functions of In_2O_3:Sn, MgF_2 and glass. The distance between a certain point on the curve and the point C describes the excitation purity of the colour (the graph corresponding to 1 % excitation purity is indicated). A full interpretation of the data in Fig. 22 is beyond the scope of these notes; it is sufficient to observe that the excitation purity (or perceived colour) is significantly decreased when an MgF_2 layer is applied. Specifically, it is found that an excitation purity of <1 % in normal transmission and <10 % in normal reflection could be achieved with In_2O_3:Sn thicknesses in the 220-260- or 335-365 nm ranges and MgF_2 thicknesses in the 90-105-nm range.

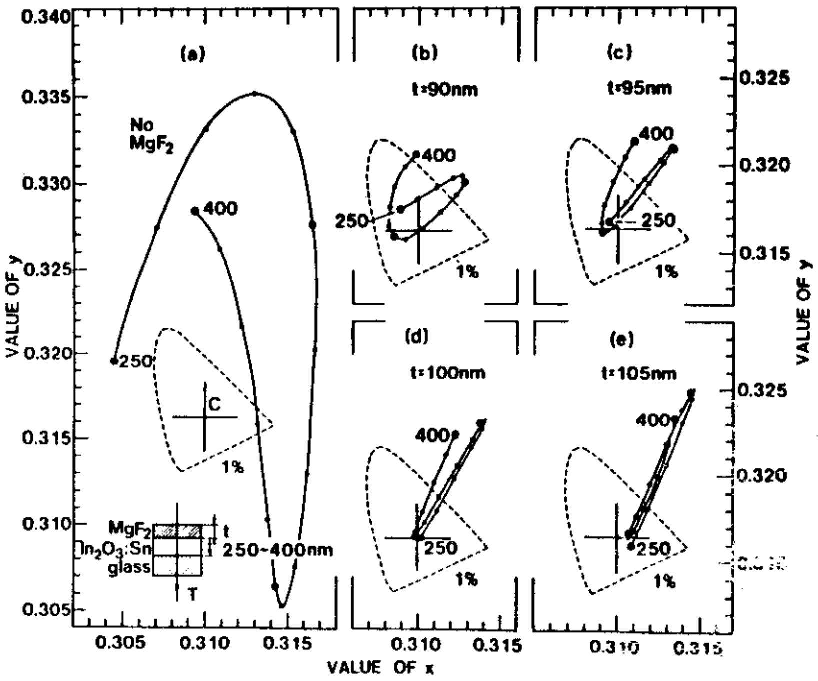

Figure 22. *Solid curves show the CIE 1931 (x,y) chromaticity coordinates for normal transmission of daylight (standard illuminant C) through an In_2O_3:Sn film antireflected by MgF_2 on glass. Chromaticities corresponding to 10-nm thickness increments of In_2O_3:Sn are marked on the curves.*

We now turn to a theoretical analysis of the optical properties of In_2O_3:Sn. To this end we regard In_2O_3 as a host lattice to which the effect of the Sn dopant is added. The bandstructure of In_2O_3 - which forms the natural basis for a theory of the optical properties - is not known in any detail, but we believe that Fig. 23 (a) gives a good working model. It shows parabolic and isotropic bands separated by a direct semiconductor bandgap E_{go}, which is 3.75 eV. It has been proposed that the conduction band is mainly from indium 5s electrons and the valence band is from oxygen 2p electrons. The Fermi energy E_F lies halfway between the energy bands. We next introduce a low density of donor atoms. Under these conditions, donor states are formed just below the conduction band, and E_F lies between the donor level and the conduction band minimum. For increased donor density, the donor states merge with the conduction band at a certain "critical" density n_c, whose magnitude can be estimated using Mott's criterion[65]

$$n_c^{1/3} a_o^* \approx 0.25 \, . \qquad (30)$$

The effective Bohr radius a_o^* is ≈ 1.3 nm for In_2O_3. Above n_c, the Sn atoms are singly ionized. E_F is determined by the highest occupied states in the conduction band. Figure 23 (b) depicts the bandstructure of heavily doped In_2O_3. A partial filling of the conduction band as well as shifts in energy of the bands, relative to their location in In_2O_3, are indicated.

As earlier discussed in Sec.2.2, it is often possible to consider the complex dielectric function as a sum of contributions due to valence electrons, free electrons, and phonons (cf. Eq.12). Below we regard the susceptibilites for these contributions for the case of In_2O_3:Sn. We begin our discussion of χ^{VE} by noting that the fundamental bandgap of a heavily doped oxide semiconductor becomes wider as the electron density n_e is increased. The shift occurs as the net result of two competing mechanisms: a bandgap widening due to a blocking of the lowest states in the conduction band (so that absorption occurs for photon energies exceeding E_g rather than W in Fig. 23), and a bandgap narrowing due to electron-electron and electron-ion scattering (so that $W<E_{g0}$ in Fig. 23). Hence bandgap widening occurs as a consequence of the Burstein-Moss effect,[66] which is pronounced because of the small effective mass for the conduction electrons in In_2O_3:Sn. The empirical data follow approximately the relation $E_g - E_{g0} \propto n_e^{2/3}$. There is also a smearing of the bandgap which increases in proportion to n_e and which may also be dominated by effects of electron scattering (rather than of nonzero

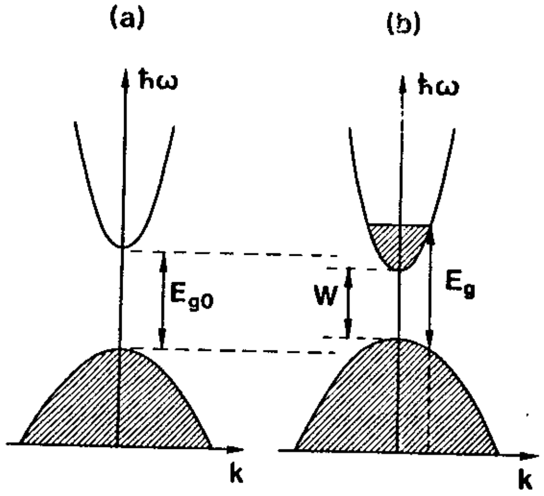

Figure 23. *Part (a) shows the assumed bandstructure of undoped In_2O_3 in the vicinity of the top of the valence band and the bottom of the conduction band. k is wavevector amplitude and ħω is photon energy. Part (b) describes the effect of Sn doping. A shift of the bands is indicated. Shaded areas denote occupied states.*

temperature). If we confine our attention to the solar range, it is sufficient to regard the low-energy tail of the bandgap. Figure 24 shows absorption coefficient, evaluated from spectrophotometric measurements, versus photon energy for films of In_2O_3 and In_2O_3:Sn. The samples denoted A, B, C, D have the thicknesses 0.075, 0.115, 0.11, and 0.41 μm, and the electron densities 0.4, 1.7, 6.2, and 8.0 x 10^{20} cm^{-3}, respectively. The n_es were obtained from optically observed screened plasma energies. Below 4 eV, the data in Fig. 24 is seen to follow approximately the relation

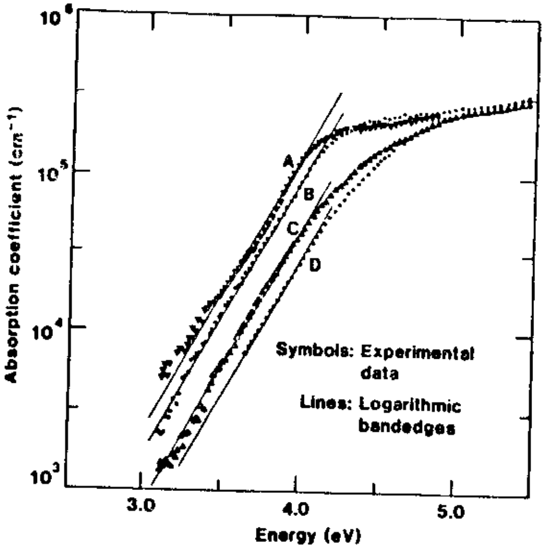

Figure 24. *Absorption coefficient versus photon energy for films of In_2O_3 and In_2O_3:Sn. Symbols refer to measurements at room temperature; the scatter illustrates the difficulty of using thin films to determine small absorption coefficients. The parallel lines indicate logarithmic band-edges.*

$$\alpha = \alpha'' \exp \left[a (\hbar\omega - b) \right], \qquad (31)$$

where α", a and b are parameters. Such logarithmic bandedges are often referred to as Urbach tails.[67] We may rewrite Eq. (31) in terms of a valence electron susceptibility, applicable in the bandedge (be) range, as

$$\chi_{be}^{VE} = \varepsilon_\infty - 1 + i\,(\varepsilon_\infty^{1/2}/2\pi)\lambda\alpha'' \exp\left[a(\hbar\omega - b)\right]. \qquad (32)$$

The bandgap shift can be represented by

$$b = c n_e^{2/3} + d, \qquad (33)$$

with c and d being parameters. The empirical results in Fig. 24 can be reproduced by setting $\alpha'' = 1\ \mathrm{cm}^{-1}$, $a = 3.99\ (\mathrm{eV})^{-1}$, $c = 0.376 \times 10^{-14}\ \mathrm{cm}^2\ \mathrm{eV}$, and d = 0.979 eV. Urbach tails may be connected with electric microfields due to the ubiquitous ionized defects[68], thermal fluctuations of the bandgap,[69] etc.

Turning to the free-electron properties, we note that the spectral selectivity required for a window coating rests to a large extent on these. The analysis of free-electron properties is conveniently performed in terms of a complex dynamic resistivity $\rho \equiv \rho_1 + i\rho_2$, which is connected with the susceptibility via the general relation

$$\chi = i/(\varepsilon_0 \omega \rho), \qquad (34)$$

where ε_0 is the permittivity of free space. This formalism is useful[70] since ρ_1 is directly related to the type of scattering which prevails amongh the free electrons. The dots and solid curves in Fig. 25 show empirical results for three heavily doped In_2O_3:Sn films with somewhat different electron

densities. The data is based on spectrophotometric measurements of transmittance and reflectance in the solar and thermal ranges. We find that ρ_1 is rather constant below the plasma energy $\hbar\omega_p$ and joins smoothly with the measured dc resistivity ρ_c. Above the plasma energy, ρ_1 falls off according to a power law. With due consideration of experimental uncertainties, it is found that a relation

$$\rho_1 \propto \omega^s, \text{ with } -1.3 \gtrsim s \gtrsim -2, \qquad (35)$$

is obeyed. At the highest energies shown in Fig. 25, ρ_1 levels off and starts to increase at the approach of the semiconductor bandgap. $-\rho_2$ also follows a power law with an exponent between 0.85 and 1.0. Additional data for $\hbar\omega < 0.1$ eV were consistent with the results in Fig. 25.

We now wish to present a quantitative theoretical model for ρ. To this end we consider ionized impurity scattering, which is unavoidable for $n_e \gg n_c$. Using the Gerlach-Grosse theory[70] appropriate to a Coulomb potential we can write

$$\rho(\omega) = i \frac{Z^2 N_i}{6\pi^2 \varepsilon_0 n_e^2 \omega} \int_0^\infty k^2 dk \left[\frac{1}{\varepsilon^{eg}(\vec{k},\omega)} - \frac{1}{\varepsilon^{eg}(\vec{k},0)} \right] - i \frac{\omega}{\varepsilon_0 \varepsilon_\infty \omega_p^2}, \qquad (36)$$

where Z is the charge of the impurities, N_i is their density, and ε^{eg} is the dielectric function of the free-electron gas. For heavily doped In_2O_3:Sn, we may set Z = 1 and $N_i = n_e$, thus assuming that the free electrons stem from singly ionized Sn atoms.[71] The remaining part of the theory regards ε^{eg}. We first consider the Random Phase Approximation[9,72](RPA). For electron collision processes it is the longitudinal part of the dielectric function that matters, and in the limit of small damping we have for the degenerate electron gas (with $\varepsilon^{eg} \equiv \varepsilon^{RPA}$)

$$\varepsilon^{RPA}(k,\omega) \equiv \varepsilon_\infty + vP(k,\omega) = \varepsilon_\infty + \frac{3\omega_p^{\ 2}}{k^2 v_F^{\ 2}} (f_1 + if_2), \tag{37}$$

where v_F if Fermi velocity. Explicit expressions for f_1 and f_2 may be found in Ref. 56. RPA is known[9] to give a good description of the free-electron gas particularly when the parameter

$$r_s{}^* = a_o{}^* \; (4\pi n_e/3)^{1/3} \tag{38}$$

is small. For heavily doped In_2O_3:Sn we can have $r_s{}^* \sim 1$. This is in fact smaller than for metals, which attests to the applicability of the RPA. Nevertheless, the RPA is not entirely satisfactory since it leaves out the effects of exchange and correlation in the electron gas, and it is of some interest to invoke more elaborate theories. One such extension of RPA, which includes exchange but not correlation, was introduced by Hubbard.[73] Within this theory, screening in the electron gas is represented (with $\varepsilon^{eg} \equiv \varepsilon^H$) by

$$\varepsilon^H(k,\omega) = \varepsilon_\infty + [\,1 - G^H(k)\,]\; vP(k,\omega), \tag{39}$$

$$G^H(k) = k^2/2(k^2 + k_F{}^2). \tag{40}$$

Here $k_F = (3\pi^2 n_e)^{1/3}$ denotes the Fermi wavevector.

The dashed curves in Fig. 25 were computed from the theory outlined above with no free parameter. We used empirical results for n_e, the Hubbard correction to the RPA, and

$$\varepsilon_\infty m_c{}^* = 1.4 \text{ m}, \tag{41}$$

where $m_c{}^*$ is the effective conduction band mass and m is the free-electron mass. The relation in Eq.(41) was taken from the detailed work by Köstlin et al.[74]

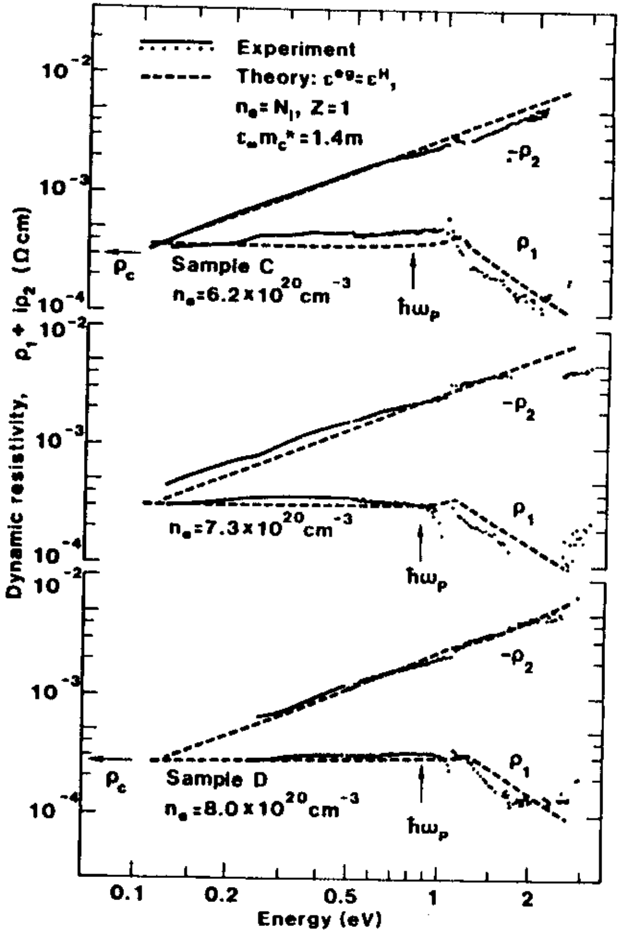

Figure 25. *Real and imaginary parts of the dynamic resistivity for In_2O_3:Sn films. Dots and solid curves were evaluated for three films. The actual spread in the data is apparent from the dots; the lines are shown for the energies where the spread is insignificant. Dashed curves were computed from the theory of ionized impurity scattering with the shown parameters. The detailed plasmon features around the "knee" in the ρ_1 data are not resolved. The pertinent values of plasma energy $\hbar\omega_p$ and dc resistivity ρ_c are indicated by arrows.*

The correspondence between theory and experiment is striking; not only the slopes of the curves but also their magnitude in the whole spectral region - from the thermal infrared and well into the visible - are in agreement. Specifically, the parameter s (cf. Eq. 35) obtained from the computation was equal to - 1.5, which is as expected from ionized impurity scattering. We thus conclude that the Gerlach-Grosse theory of ionized impurity scattering, with screening in the electron gas represented by the RPA or an extention thereof, provides a quantitative model for the free-electron properties of high-quality In_2O_3:Sn films produced by reactive e-beam deposition. The crystallite size of the analyzed coatings is ~ 50 nm, which is an order of magnitude larger than the mean free path due to ionized impurity scattering below the plasma energy. Above $\hbar\omega_p$, the ions become less efficient scatterers, and in the visible spectral range it may be that defect scattering is not negligible. To account for this possibility one may use the provisional formula

$$\chi^{FC} = \frac{i}{\varepsilon_0\omega \quad \rho(\omega)} + i\eta, \qquad (42)$$

with ρ taken to represent ionized impurity scattering only. For the coatings considered here, it appears that $\eta \approx 0.01$. In general, η can be regarded as a quality factor whose magnitude depends on the fabrication technique.

We consider phonon absorption and present in Fig. 26 spectrophotometric reflectance data for an In_2O_3 film. The spectrum, given on a wavenumber axis, displays three main peaks at 330, 365 and 412 cm^{-1}. Shoulders on these peaks, as well as smaller features at higher wavenumbers, are apparent. All of these structures are believed to correspond to damped transverse phonon-polaritons, whose effect on the optical data is a reflectance maximum. The longitudinal polariton coincides with the plasmon resonance, which is a consequence of the free electrons in In_2O_3. In In_2O_3:Sn, the added free electrons effectively

screen out the transverse polaritons, so that hardly any observable structure remains in the spectra. According to White and Keramidas,[75] a factor group analysis predicts 16 infrared active modes in In_2O_3. It appears that 9 of these can be identified in the spectra. We may represent χ^{PH} by a sum of three damped Lorentz oscillators (cf. Eq. 13) according to

$$\chi^{PH} = \sum_{j=1}^{3} \frac{\Omega_j^{PH}}{(\omega_j^{PH})^2 - \omega^2 - i\omega\Gamma_j^{PH}} \quad . \qquad (43)$$

For j = 1,2,3, ω_j^{PH} takes the values 412, 365, and 330 cm^{-1}, Ω_j^{PH} takes the values 330, 600, and 450 cm^{-1}, and Γ_j^{PH} takes the values 5, 12, and 16 cm^{-1}.

Equations (12), (32), (42) and (43) specify the dielectric function of In_2O_3:Sn, from which one can compute transmittance, reflectance, emittance, etc. In the first calculations reported below we took the In_2O_3:Sn films to be backed by a medium characterized by a constant refractive index equal to 1.5. This simulates a substrate of glass with low Fe_2O_3 content in the visible and near-infrared, or a foil of a polymer such as polyester, polyethylene, etc. In subsequent calculations we represented the substrate by the dielectric function of amorphous SiO_2.[52] Figure 27 shows spectral normal transmittance and reflectance for a 0.2 - µm - thick film with $10^{20} \leq n_e \leq 3 \times 10^{21}$ cm^{-3}. The bandgap widening, the onset of strong reflectance at a wavelength which scales with n_e, and a gradual disappearance of the phonon-induced structure are all clearly seen. At $n_e = 6 \times 10^{20}$ cm^{-3}, we find high solar transmittance combined with high thermal-infrared reflectance, and we conclude that such coatings are of interest as low emittance window coatings. Setting $n_e = 3 \times 10^{21}$ cm^{-3} we have high luminous transmittance and high near-infrared reflectance, which is the desired property for a solar-control coating. However, coatings with $n_e \gtrsim 10^{21}$ cm^{-3} cannot be produced. Excessive doping yields unwanted absorption due to various Sn-based complexes,[71] so that the theoretical model breaks down for the highest electron densities considered in Fig. 27.

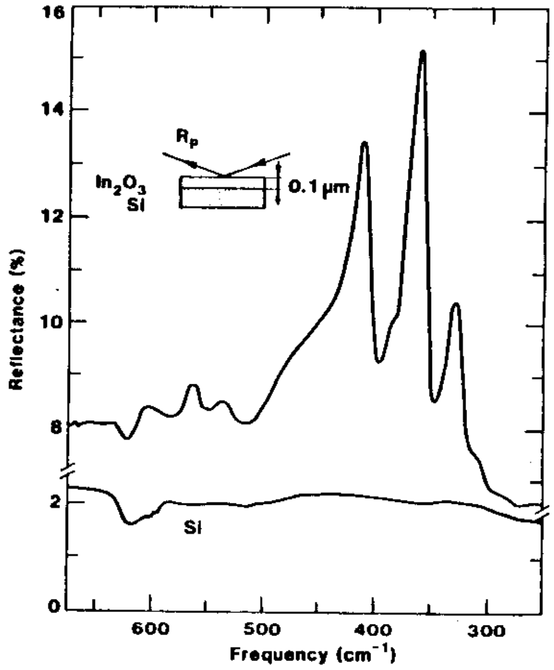

Figure 26. *Spectral reflectance of a bare Si substrate (lower curve) and after coating it with a 0.1 μm thick film of* In_2O_3 *(upper curve) whose electron density was* $\sim 0.5 \times 10^{20}$ cm^{-3}. *The optical measurement used 70° angle of incidence and p-polarised light. The experimental configuration is shown in the inset.*

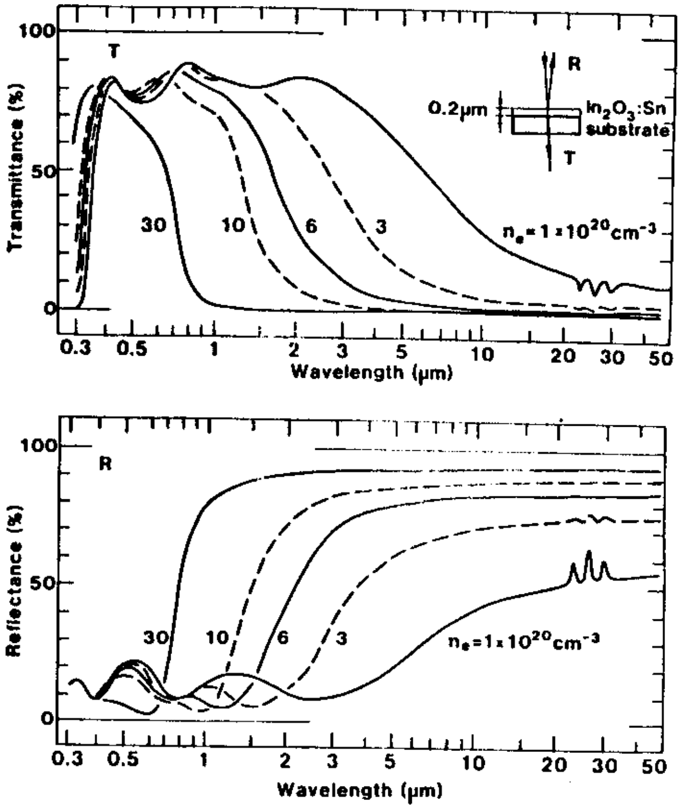

Figure 27. *Spectral normal transmittance (upper part) and reflectance (lower part) as computed from the model for the optical properties of* In_2O_3:*Sn. The shown values of electron density and film thickness were used.*

We have now a sufficient background to assess the In_2O_3:Sn films for use on energy-efficient windows. To this end we need integrated luminous, solar and thermal quantities, which were derived from the spectral data by use of the formulas given in Sec. 3.2. Figure 28 shows T_{lum} and R_{lum} for In_2O_3:Sn coatings with four thicknesses and $10^{20} \leq n_e \leq 3 \times 10^{21}$ cm^{-3}. At $n_e < 10^{21}$ cm^{-3} we find $75 \leq T_{lum} \leq 85$ % and $10 \leq R_{lum} \leq 20$ %; the actual magnitudes of these quantities are strongly influenced by optical interference. As the electron density goes up, there is a tendency for R_{lum} to decrease while T_{lum} varies in a more erratic manner. Figure 29 is the counterpart for T_{sol} and R_{sol}. It is seen that T_{sol} decreases and R_{sol} increases when n_e goes up. This can be interpreted as a result of the plasma wavelength which gradually moves into the solar spectrum from the infrared side. At $n_e \lesssim 5 \times 10^{20}$ cm^{-3} we have $R_{sol} \approx 13$ % irrespective of film thickness. Figure 30 reports on hemispherical thermal emittance. The solid curves were computed for In_2O_3:Sn films backed by a non-emissive material having a refractive index of 1.5. In order to make valid assessments for a glass

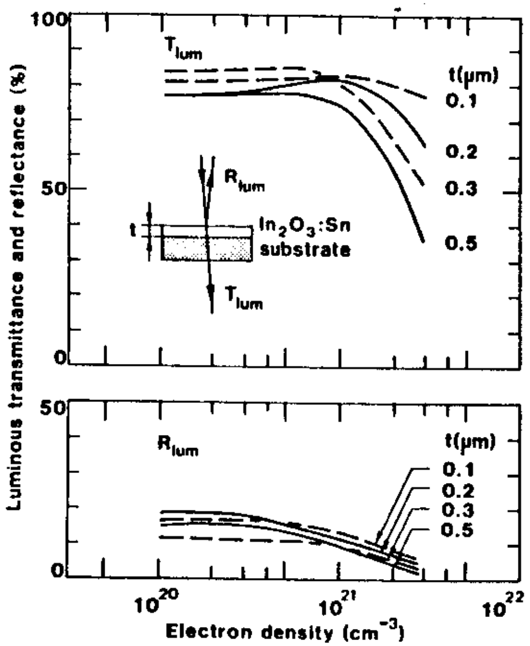

Figure 28. *Luminous normal transmittance (upper part) and reflectance (lower part) versus electron density as computed from the model for the optical properties of In_2O_3:Sn. Results are shown for four film thicknesses.*

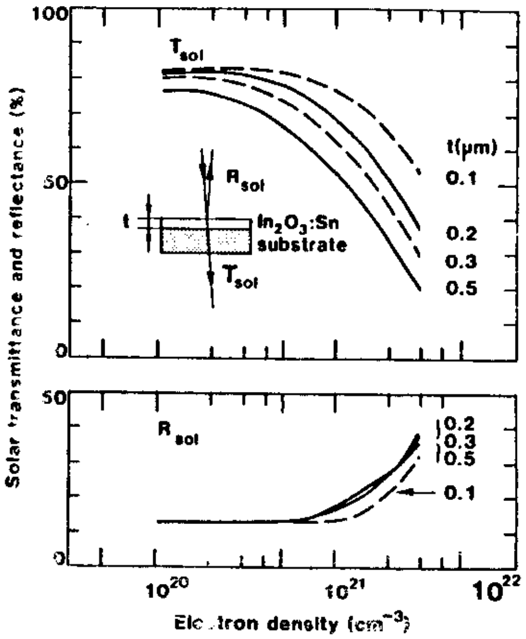

Figure 29. *Solar normal transmittance (upper part) and reflectance (lower part) versus electron density as computed from the model for the optical properties of In_2O_3:Sn. Results are shown for four film thicknesses. The curves for R_{sol} corresponding to 0.2, 0.3 and 0.5 µm thick films are almost overlapping.*

window, we also studied a configuration with an intermediate SiO_2-layer which was sufficiently thick so as to simulate bulk-like properties. The dotted curves in Fig. 30 pertain to this latter configuration. Generally, there is a decrease in the emittance as the electron density and the film thickness increase, which is a direct consequence of the increased number of free electrons. We conclude from Fig. 30 that substrate emission is important for $n_e \lesssim 5 \times 10^{20}$ cm^{-3}, but negligible above this electron density provided that the In_2O_3:Sn films are thicker than ~0.2 µm. This latter films have $E_{therm} \lesssim 15$ % for $n_e \approx 10^{21}$ cm^{-3}.

Figures 28-30 show that In_2O_3:Sn films can combine high transmittance of luminous and solar radiation with low thermal emittance, and consequently they are useful for energy efficient windows. A fully quantitative optimization is outside the scope of these notes, but it is nevertheless possible to draw some general conclusions. To this end we first fix E_{therm} at a low value. It is not meaningful to diminish it to the extreme, since conductive and convective heat transfer cannot be eliminated in an ordinary gas-filled unit. Specifically, we took E_{therm} to be 15, 20 and 25 %. The dotted curves in Fig. 30 yield corresponding electron densities for the investigated film thicknesses, and the pertinent values of T_{sol} can be read from Fig. 29. Figure 31 displays solar transmittance as a function of film thickness with E_{therm} as parameter. Requiring $E_{therm} = 15$ % one cannot exceed $T_{sol} \approx 70$ %, which is undesirably low for many applications. On the other hand, limiting the requirement to $E_{therm} = 20$ %, one can have $T_{sol} \approx 78$ %. At still larger values of E_{therm} it is possible to reach a marginally improved solar transmittance. Optimum performance can be obtained with 0.2 - µm - thick In_2O_3:Sn films having $4 \leq n_e \lesssim 6 \times 10^{20}$ cm^{-3}. Spectral data for such a film was shown in Fig. 27. The optimization of the luminous transmittance and the colour properties can be regarded as a separate problem, whose solution rests on antireflection treatments. These aspects were discussed in Sec. 4.2.

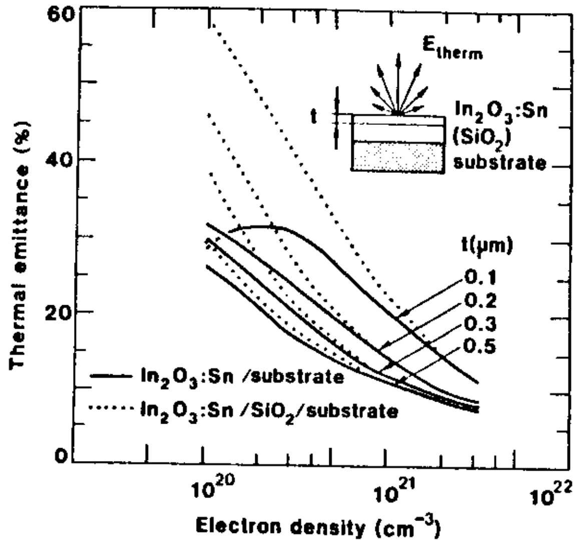

Figure 30. Thermal hemispherical emittance versus electron density as computed from the model for the optical properties of In_2O_3:Sn. The substrate is taken to be non-emitting with a refractive index equal to 1.5 (solid curves) or having properties given by the dielectric function of amorphous SiO_2 (dotted curves). The shown film thicknesses were used.

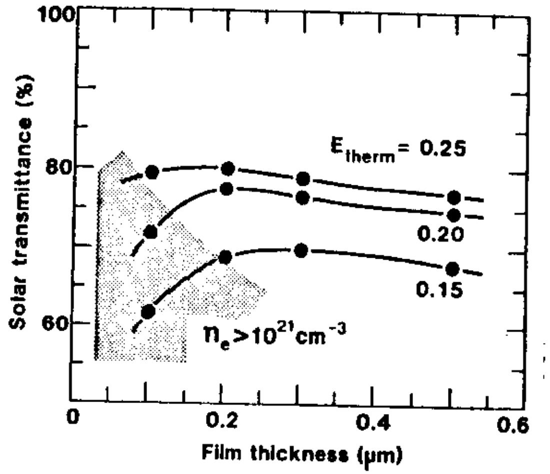

Figure 31. *Normal solar transmittance versus film thickness for three values of hemispherical thermal emittance, as computed from the model for the optical properties of In_2O_3:Sn and with the substrate represented by the dielectric function for amorphous SiO_2. Curves are drawn only to guide the eye. The shaded area refers to films with $n_e > 10^{21}$ cm^{-3}, which cannot be produced experimentally,*

4.5 Optical itching coatings for windows

Most of this se on will be devoted to inorganic electrochromic coatings. At the end we i ude some results for thermochromic coatings. Electrochromism, i.e. persistent change of the optical properties under the action of an el tric field, is wellknown in oxides based on W, Mo, Ir, Ni and others, as l as in numerous organic materials. Earlier work, mainly oriented towards non-emissive information displays, is surveyed in Refs. 44 and 76-79. Here we first make some general remarks as to the design of an electrochromic w ndow coating and then discuss results for crystalline WO_3, amorphous WO_3, and for NiO_x.

An electrochromi coating for use on a "smart window" (i.e., a window whose optical performa ce can be altered in accordance with dynamic needs for heating and cool ng) must encompass several materials. Figure 32 sketches a basic configuration which is convenient for discussing the operating principles. It comprises two transparent conducting layers, required for applying the ele tric field, and intervening materials serving as active electrochromic l yer, ion conductor, and ion storage. The optical properties of the electroch omic material change under insertion or withdrawal of ions. Either of the transparent electrodes can be a heavily doped oxide semiconductor or, possibly, a semitransparent metal film. These latter materials were discussed a length in Secs.4.2-4.4. The ions needed in the electrochromic reaction are provided by the ion storage and are injected into, or withdrawn from, e electrochromic layer via the ion conductor. The detailed design can be of ifferent types: for devices using liquid electrolytes the electrolyte can rve both as storage and conductor for the ions, while in all-solid-state devices the ion conductor can be an appropriate dielectric and the ion storage can be another electrochromic layer (preferably anodic if the base elec rochromic layer is cathodic, or vice versa). One may also combine the conductor and storage media into one layer. Further it is possible to exclude the ion storage medium and instead rely on a replenishment of H^+ ions, originating from the dissociation of water molecules diffusing in from an ambience with controlled humidity; obviously, this requires a substantial atomic permeability of the outer electrode.

The radiative properties of a "smart window" are switchable between different states. The nature of this switching can be different depending on the basic requirement on the window, i.e., whether the main goal is to achieve control of the energy flowing through the window aperture, or if daylighting and glare control are of prime importance. Under certain conditions it may also be possible to have variable thermal insulation. In Fig. 33 we illustrate idealized cases for energy control. For this application it is important to remember that the solar spectrum extends over the 0.3-3-μm range, whereas the eye is sensitive only in the 0.4-0.7-μm interval. The pertinent spectra are shown by the shaded areas in Fig. 33; they were illustrated also in Figs. 7 and 8. Almost 50 % of the total solar energy comes as infrared radiation, and hence it is possible - at least in principle - to change the energy throughput within rather wide limits without affecting the luminous transparency. The changed infrared transmittance can be achieved in two ways: by modulating the infrared reflectance as indicated in the upper part of Fig. 33, or by modulating the infrared absorptance as indicated in the lower part. A gradual decrease in the transmitted energy is obtained as the reflectance edge moves towards shorter wavelength, or as the absorptance goes up. Both types of modulation occur in electrochromic WO_3 as we will see shortly: the properties of crystalline WO_3 films are conveniently treated in terms of modulated reflectance, whereas amorphous WO_3 displays modulated absorptance. The thermal properties of the "smart windows" are governed by

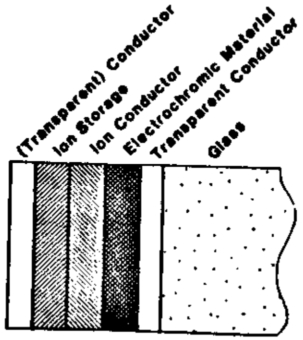

Figure 32. Basic design of an electrochromic coating for "smart windows".

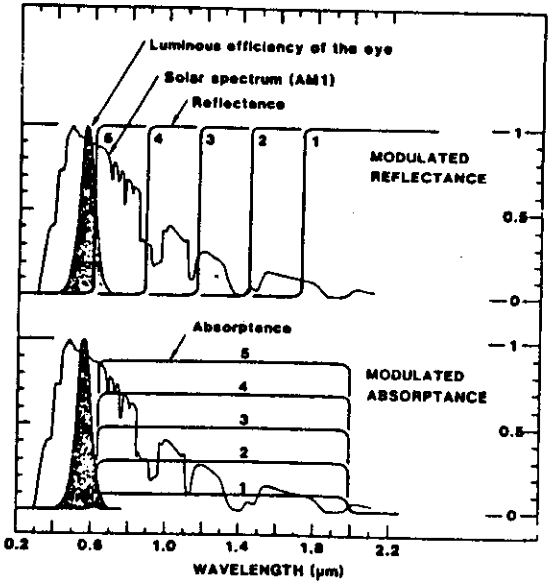

Figure 33. Optical properties of idealized switching coatings for controlled energy throughput in "smart windows". The performance with modulated reflectance and modulated absorptance as working principles are shown (the spectral position of the absorption band is somewhat arbitrary). Shaded areas denote the luminous effeciency of the eye and a typical solar irradiance spectrum.

their reflectance in the 3-100-μm range. The all-solid-state concept, which is preferable in a window, includes an extended outer transparent conductor which provides low thermal emittance. In many cases this is the desired property. If instead a high thermal emittance is required, this can be obtained by applying a suitable external coating to the electrochromic multilayer structure.

We now consider crystalline electrochromic WO_3. The reversible colouring and bleaching is generally believed[76] to be the result of a double injection of positive ions (M^+) and electrons (e^-) according to the overall reaction

$$xM^+ + xe^- + WO_{3-y} \rightleftarrows M_xWO_{3-y}, \qquad (44)$$

with $0 < x \leq 0.5$ and $y \leq 0.03$. The optical properties can be understood qualitatively from the formation of an electron gas. Since each injected

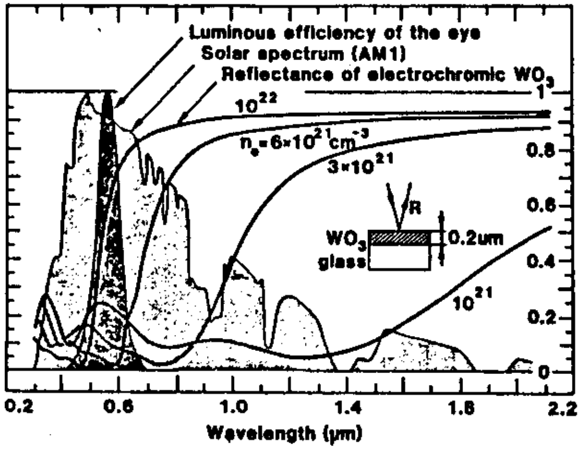

Figure 34. *Computed spectral reflectance for crystalline electrochromic WO_3 films with different electron densities. Solar and luminous spectra are shown.*

ion is associated with one electron, it is possible to compute the limiting performance of an electrochromic window coating including crystalline WO_3 by considering only the inevitable ionized impurity scattering, and disregarding the role of all layers except the electrochromic one. With this premise, one can apply precisely the same theory as the one used to treat the free-electron properties of In_2O_3:Sn in Sec. 4.4. We set $\varepsilon_\infty = 4.8$, $Z = 1$ and $m_c^* = 0.5\ m$. Figure 34, reproduced from Ref. 80, shows some typical data for computed spectral reflectance. The results pertain to a 0.2 μm thick electrochromic WO_3 film with $10^{21} \leq n_e \leq 10^{22}$ cm^{-3}, backed by a glass substrate whose refractive index was put at 1.53. With increasing n_e, the onset of strong reflectance is shifted towards shorter wavelength and the transition becomes progressively sharper. This follows from an altered plasma wavelength. The results may be appreciated by comparing them with characteristic spectra for sunlight and for the luminous efficiency of the eye (shaded areas). The potential for varying the reflection and transmission of infrared sunlight is apparent; quantitative data are given in Ref. 80. Experimental data on crystalline WO_3 have been published in Refs. 81 and 82.

We now turn to amorphous WO_3 films and discuss some recent experiments.[83,84] Also in this case, the colouring can be understood from the double injection model in Eq. 44. The first design comprises a glass substrate, made electrically conducting by an In_2O_3:Sn film, coated with a 0.3-μm-thick layer prepared by reactive e-beam deposition of WO_3. This sample was mounted so that it formed the working electrode in a transparent electrochemical cell containing a small Pt counter-electrode, and a liquid electrolyte of 1 M $LiClO_4$ in $C_4H_6O_3$. The sample was connected in a standard three-electrode potentiostatic configuration, with a saturated calomel reference electrode. The whole cell was put in the sample compartment of a spectrophotometer.

An analogous cell, containing electrolyte but no glass sample, was put in the reference beam. Transmittance was recorded in the 0.35-1.3-µm-range. In the combined electrical and optical measurements, we first applied a voltage between the working electrode and reference electrode until maximum transmittance was observed. The WO_3 layers were then coloured, by gradually forming Li_xWO_3, through a reversal of the voltage. The colouring was halted at intermediate levels in the colour-bleach cycle and corresponding transmittance spectra and voltages (V; measured between the working electrode and the reference electrode) were recorded. Figure 35 shows a typical set of curves. Large changes of the optical properties are seen to occur as a result of a low voltage. The devices exhibit open-circuit memory. The

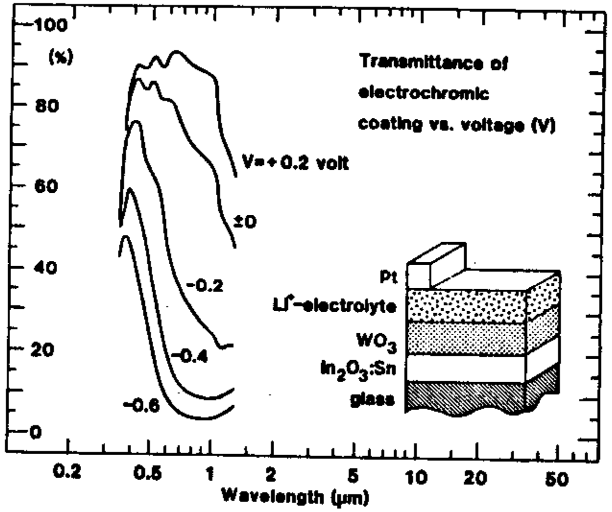

Figure 35. *Normal spectral transmittance as a function of voltage for an electrochromic configuration with a glass substrate, coated with In_2O_3:Sn and WO_3, immersed in a liquid Li^+-electrolyte.*

integrated solar transmittance obtained from Fig. 35 lies between 86 and 12 %.

All-solid-state devices are preferrable for practical purposes, and the first prototype products of this kind have been announced. Here we describe some work of ours.[84] The specimen consists of - in order - In_2O_3:Sn, 0.15 µm of WO_3 produced by evaporation in the presence of O_2, 0.05 to 0.1 µm of MgF_2 produced by evaporation in the presence of water vapour, and Au. The top electrode is ~ 15 nm thick and hence semitransparent at short wavelengths. As a voltage (V) is applied between the In_2O_3:Sn and Au films, the transmittance is changed. This may be caused by dissociation of H_2O molecules and subsequent formation of H_xWO_3. Figure 36 shows some initial data on

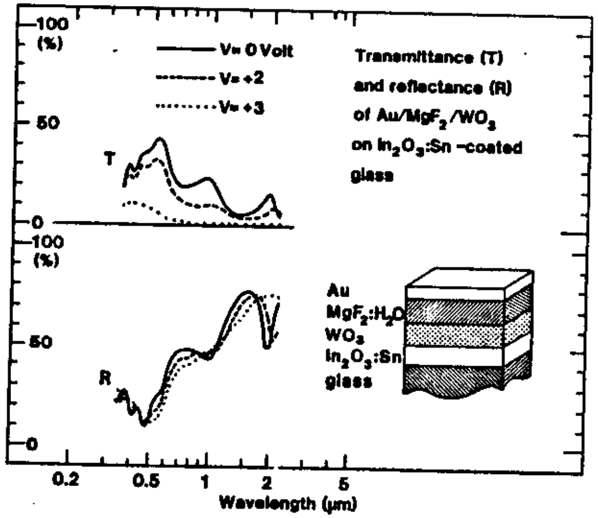

Figure 36. *Normal spectral transmittance and reflectance as a function of voltage for a glass substrate covered with a multilayer stack of In_2O_3:Sn, WO_3, MgF_2 and semitransparent Au.*

variable transmittance and reflectance in the 0.35-2.2-μm interval. The corresponding integrated solar transmittance varies between 25 and 3 % when the voltage is altered. The durability of these coatings is not yet satisfactory for practical use, and storage in dry air tends to deteriorate the electrochromic property.

Generally speaking, durability may be a problem for WO_3-based devices, and there is a need to have alternative electrochromic materials. One such alternative is hydrated nickel oxide.[85,86] The inset of Fig. 37 shows a sample configuration recently investigated by us.[86] A glass plate with an In_2O_3:Sn film was coated with NiO_x by use of reactive rf-magnetron sputtering. The samples were bleached and coloured during immersion in 1M KOH. It appeared that the electrochromic reaction[87] could be written, schematically, as

$$\mathrm{Ni\,(OH)_2} \underset{\text{bleach}}{\overset{\text{colour}}{\rightleftarrows}} \mathrm{NiOOH} + H^+ + e^- . \tag{45}$$

Thus colouring is associated with hydrogen extraction (rather than hydrogen insertion as for WO_3). Figure 37 shows normal transmittance T and near-normal reflectance R in the $0.35 < \lambda < 2.5$μm wavelength interval. The initial bleached film had T ~ 75 % and R ~ 15 % in the mid-luminous range ($\lambda \approx 0.55$μm), as indicated by the dotted curves. The performance remained almost unchanged after ~ 10^4 colour-bleach cycles, as apparent from the solid curves. Typical properties of a heavily coloured sample are given by the dashed curves, which were obtained for a sample from which 150 mC had been extracted. Now T ~ 12 % and R ~ 6 % at $\lambda \approx 0.55$μm. The large optical modulation as well as the extreme durability of the coatings are noteworthy. The window performance of the coatings was assessed by evaluating the integrated solar and luminous transmittance by the formulas given in Sec.3.2. Figure 38 reports T_{sol} and T_{lum} versus extracted charge as obtained from the

spectral normal transmittance data. A monotonic decrease of the integrated transmittance is found with T_{sol} going from ~ 75 % to ~ 20 % and T_{lum} going from ~ 75 % to ≤ 10 % when the charge extraction is increased to 200 mC. The rate of change for T_{sol} and T_{lum} is largest for small amounts of extracted charge.

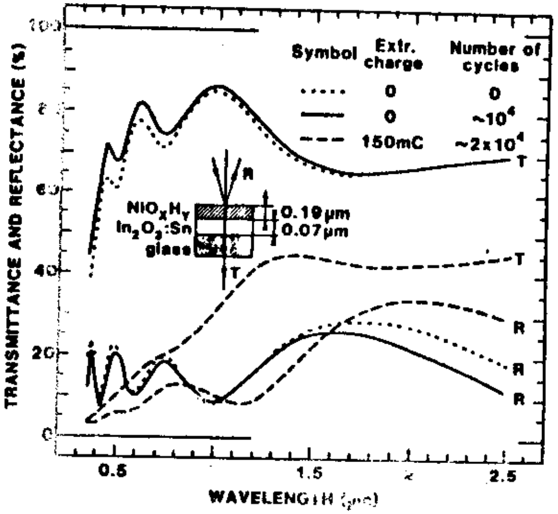

Figure 37. Spectral transmittance at normal incidence and reflectance at 10° angle of incidence for an electrochromic NiO_x-based layer on In_2O_3:Sn-coated glass. The curves refer to different magnitudes of extracted charge and number of color-bleach cycles. The sample configuration is sketched in the inset.

We end this section with some results from our laboratory on thermochromic VO_2 coatings. Earlier work on thermochromic coatings is surveyed in Ref. 88. It is known that VO_2 undergoes a metal-insulator transition at 68°C. The transition temperature can be depressed by alloying. Figure 39 shows spectral transmittance in the 0.35-2.5μm range for a 0.2μm thick VO_2 film above and below the metal-insulator transition, as taken from Ref. 89. The sample was prepared by e-beam deposition of V metal at a substrate temperature of 310°C and at a rate of 0.2 nms^{-1}, followed by an anneal in 0.2 Torr of air at 400°C for 30h. It is seen that the solar transmittance is considerably higher at a low temperature than at a high temperature. Thus it appears to be feasible to produce thermochromic window coatings based on VO_2.

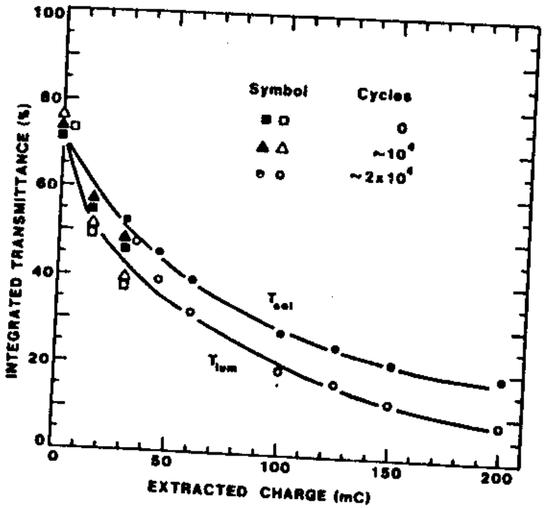

Figure 38. *Integrated solar (filled symbols) and luminous (open symbols) transmittance for electrochromic* NiO_x*-based coatings according to the inset of Fig. 37. Squares, triangles and circles refer to 0,* ~ 10^4*, and* ~ 2×10^4 *colour-bleach cycles, respectively. The curves are drawn only as a guide to the eye. A further decrease of the transmittance was observed for 500 mC extracted charge.*

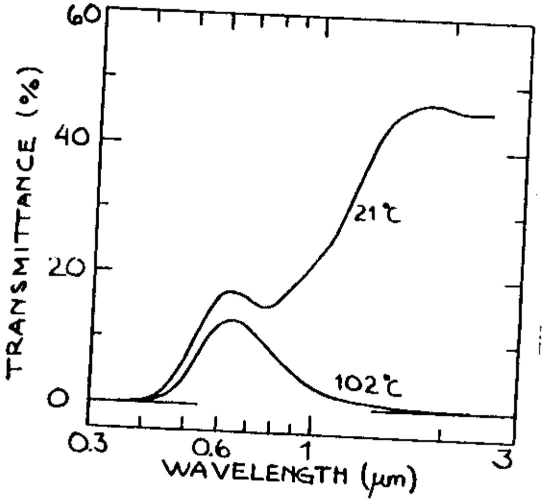

Figure 39. *Spectral transmittance of a thermochromic* VO_2 *coating at the indicated temperatures.*

5. SURFACES FOR SELECTIVE ABSORPTION OF SOLAR ENERGY

5.1 Spectral selectivity and review of coatings

It is evident from Fig. 7 that solar radiation comes at wavelengths $\lambda \leq 3\mu m$. A solar collecting surface must absorb this radiation. The surface then heats up and emits thermal radiation at $\lambda \geq 3\mu m$. This reradiation must be avoided if the solar collector is to operate at high temperatures; hence the emittance should be low for $\lambda \geq 3\mu m$. We are then led to consider selectively solar-absorbing surfaces *with low reflectance at* $\lambda \leq 3\mu m$ *and high reflectance at* $\lambda \geq 3\mu m$. Surfaces with this property do not exist in nature. Therefore - as expected from their large practical importance - they have been subject to many vigorous development programs in laboratories around the world during the last decade. The interest was rather low in the 50's and 60's but rapidly went up during the 70's. The increase was triggered by the "oil crisis" in 1973, which made the industrialized world aware of the importance of the old (known as "alternative") energy sources. Around 1980 about 100 scientific papers were published each year on selectively solar-absorbing surfaces. Although we are not able to substantiate our contention by solid numbers, it is felt that the pure research activities are now declining, and that selectively solar-absorbing surfaces enter the stage of established technology.

Reviews on selectively solar-absorbing surfaces are found in Refs. 90-99. An annotated bibliography, covering the period 1955-1981, has appeared recently.[100] It lists 565 scientific papers, including studies of almost 280 different coatings or surface treatments.

It is possible to exploit several different physical mechanisms in order to create selectively solar-absorbing coatings. The most straight-forward of these is to use a material whose *intrinsic optical properties* display the

desired kind of spectral selectivity. Generally speaking, this approach has not been very fruitful, but work[101] on ZrB_2 and some other compounds indicate that intrinsically selective materials exist.

Semiconductor-metal tandems can give the desired spectral selectivity by absorbing short-wavelength radiation in a semiconductor whose bandgap is ~ 0.6 eV and having low thermal emittance as a result of the underlying metal. The useful semiconductors have undesirably large refractive indices, which would tend to yield high reflection losses. Hence it is needed to antireflect the surfaces in the range of solar radiation. The most well known work in this category is that of the University of Arizona group, who have reported[102-104] extensively on Si-based designs prepared by chemical vapour deposition.

Multilayer absorbers can be tailored so that they become efficient selective absorbers of solar radiation. It is comparatively easy to compute their optical performance, which facilitates optimization of the designs. One interesting example is $Al_2O_3/Mo/Al_2O_3$, which was orginally developed within the US space program. This type of surface has recently been produced by large-area magnetron sputtering.[105]

Metal-dielectric composite coatings consist of very fine metal particles in a dielectric host. The ensuing optical properties can be intermediate between those of the metal and of the dielectric, as discussed in Sec.2.3. The metal-dielectric concept offers a high degree of flexibility, and the optimization of the solar selectivity can be made with regard to the choice of constituents (which also affects the microgeometry), coating thickness, and particle concentration (which may be graded), size, shape, and orientation. The solar absorptance can be improved by use of suitable substrate materials and antireflection treatments. The composite coatings can be produced by a variety of techniques such as electroplating to produce "black chrome",[106] anodization of zinc sheet,[107] inorganic colouration of anodized aluminium sheet,[108] chemical vapour deposition to make "black molybdenum",[109] and co-deposition of metal and insulator by evaporation and sputtering. Codeposited coatings are discussed in Ref. 110 and papers cited therein. We return to some of these coatings below.

The final approach to be considered here is the *textured surface absorbers*. Their high solar absorptance is induced by multiple reflections against metal dendrites which are ~ 2μm apart, while the long-wavelength emittance is rather unaffected by this texture. Wellknown examples are dendritic tungsten prepared by chemical vapour deposition[111] and textured copper, nickel and stainless steel surfaces made by sputter-etching.[112]

Only a few of the investigated selectively solar absorbing surfaces have reached commercialization. All of these obtain their desired radiative properties by a combination of two or more of the aforementioned physical mechanisms. The commercial coating which seems to be most fully understood from basic principles is nickel pigmented anodic aluminium oxide.[108] It is produced by dc anodization in dilute phosphoric acid followed by black colouration via ac electrolysis in a bath containing $NiSO_4$. The inset in Fig. 40 depicts the ensuing coating structure, as revealed by a variety of experimental techniques including electron microscopy, Auger depth profiling, and atomic absorption analysis. The Al_2O_3 forms a porous 0.7 - μm - thick structure some of which is filled with Ni particles (layer 3). The porous coating is separated from the underlying sheet Al by a compact "barrier" (layer 4). The Ni content in layer 3 is ~ 23 vol. %. The hemispherical reflectance is shown in the main part of Fig. 40. Experimental data (solid curve) is rather close to the ideal spectral profile (dotted lines). Dashed curve was computed from the Bruggeman effective-medium theory. The solar absorptance of these surfaces

is 93 to 96 % and the corresponding thermal emittance is 10 to 20 %.

The most widely used selectively solar-absorbing surface seems to be "black chrome",[106] which is a complex composite of metallic Cr and non-metallic Cr_2O_3. The metal concentration is low at the interface towards air and goes up with increasing depth within the coating. The outer surface is rough. Different preparation conditions lead to somewhat different properties.[113] Figure 41 shows spectrally selective reflectance of black chrome coatings on substrates of Ni (data by McDonald and by Mar et al.) and of Cu (data by Driver et al.). These results, which were obtained on electroplated coatings, are compared with measurements on cosputtered $Cr-Cr_2O_3$

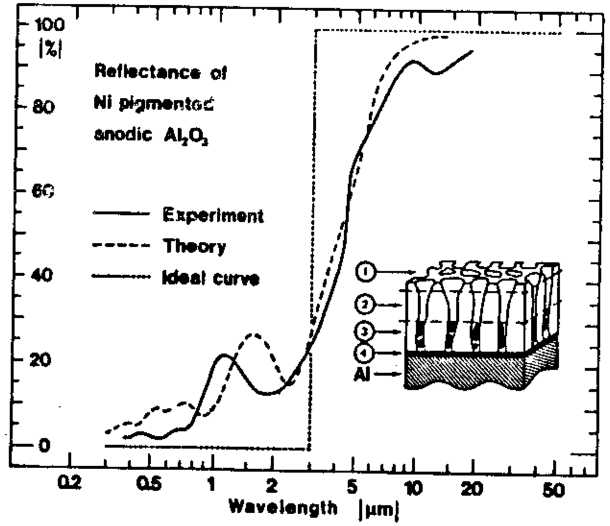

Figure 40. Spectral reflectance of a Ni-pigmented anodic Al_2O_3 coating on Al. Experimental and theoretical data are reported and compared with the ideal spectral profile. Inset depicts the coating structure.

composite films (also known as "cermets"). Reactively evaporated Cr - Cr_2O_3 coatings are also produced on a commercial scale.

Other commercial coatings or surface treatments include chemically treated rough Ni surfaces (known as MAXORB; Ref. 118), "black nickel" made by electroplating,[115, 119] graded stainless-steel carbon coatings developed for high-performance tubular solar collectors,[120] copper oxide coatings,[121] and metal-filled coloured stainless steel surfaces.[122] Work on selectively solar-absorbing paints are worth noting since it holds prospects for extremely cheap surfaces.[123,124]

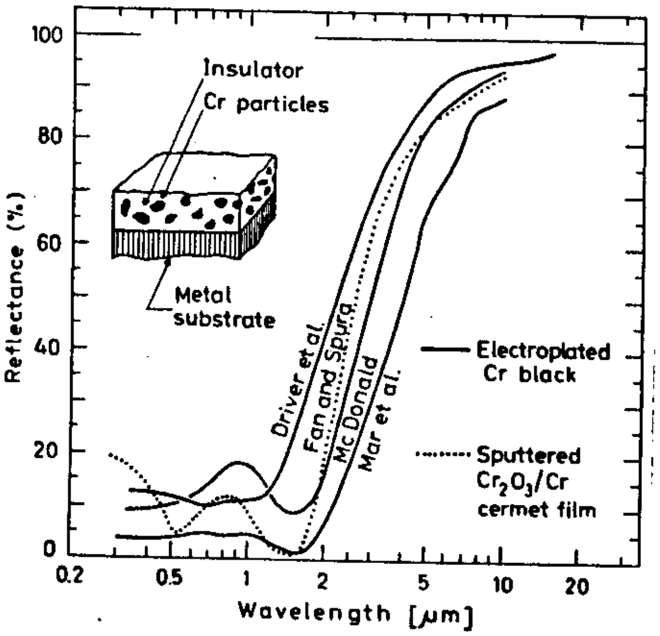

Figure 41. Spectral reflectance of "black chrome" coatings. The data are taken from McDonald (Ref. 114), Mar et al. (Ref. 115), Driver et al. (Ref. 116), and Fan and Spura (Ref.117). Inset sketches the coating structure.

5.2 Case study three: Selective absorption of solar energy in coevaporated Co-Al_2O_3 composite films (Ref. 110).

Coatings of coevaporated Co-Al_2O_3 have been investigated in great detail, and the optical properties and solar selectivity have been analyzed and compared with EMTs. This may serve as a case study illustrating the pertinent characterization and analysis techniques, the degree of theoretical understanding which can be achieved, and the use of theoretical input data in the design and production of optimized selectively solar-absorbing coatings.

The coatings were made by coevaporation of Co and Al_2O_3 in a dual e-beam system with accurate process controls. The unit, shown in Fig. 42, is in essence the same as the one described in Figs. 13 and 20. Vibrating quartz microbalances were used to obtain individual rate control of the vapour beams and hence control of the composition of the film which was formed on the substrate. The power on the e-beam sources was set by signals from the microbalances, and the system could be run via computer control. Coatings with thicknesses between 50 nm and 2 μm were produced.

The microstructure of the Co-Al_2O_3 composites was studied by high-resolution transmission electron microscopy. Figure 43 shows results for a coating with ~ 30 vol.% metal obtained in bright-field and dark-field modes. It is evident that a separated -grain structure is formed with rounded Co particles embedded in an Al_2O_3 matrix. Electron-diffraction studies showed that the particles consisted of single-crystalline hcp cobalt. The composition of the Co-Al_2O_3 was determined by a technique based on stylus measurements. Compositional depth profiles were taken by use of Auger depth profiling, secondary ion mass spectroscopy, and Rutherford back scattering. Electrical measurements gave independent information on the microstructure.

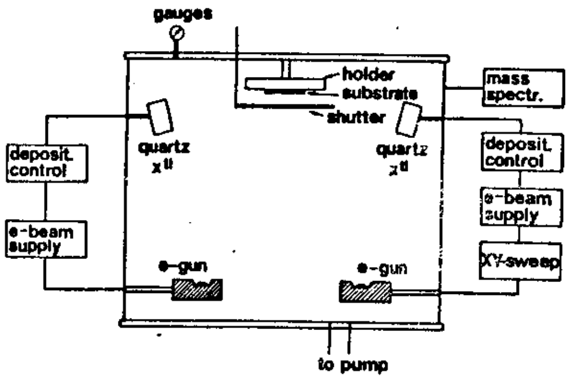

Figure 42. *Schematic view of the dual e-beam evaporation unit and the process controls.*

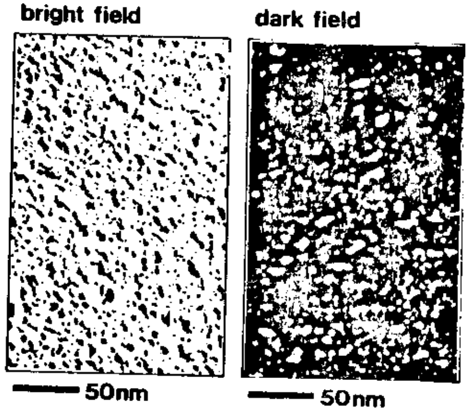

Figure 43. *Electron micrographs of a coevaporated Co-Al_2O_3 film.*

Optical data on the coatings were measured by spectrophotometry in the 0.3 - 40 - μm range. These results were used to evaluate the complex dielectric function $\bar{\varepsilon}$ by the techniques outlined in Sec. 2.4. This function is of interest for several reasons: it allows reliable comparisons with EMT-based calculations and hence makes it possible to understand the optical properties from basic principles, and it forms the natural starting point for computing the solar absorptance and thermal emittance and hence for computer-based optimizations of the solar selectivity. Figure 44 shows $\bar{\varepsilon} \equiv \bar{\varepsilon}_1 + i\bar{\varepsilon}_2$ for Co-Al_2O_3 composites with two experimentally determined volume fractions of Co (denoted f_{exp}). The high magnitude of $\bar{\varepsilon}_2$ (i.e., the high absorption) for $\lambda \gtrsim 10$ μm is due to absorption in the Al_2O_3 matrix. The dashed and dotted curves were obtained by using the Maxwell Garnett EMT together with bulk data for Co and for Al_2O_3. This particular EMT is adequate on account of the observed separated-grain topology. The Co content used in the calculations (denoted f_{th}) should be taken to have a value somewhat less than the experimental one if best agreement is to be achieved. We interpret this as evidence that ~ 5 vol. % of the Co is dispersed in the oxide matrix rather than occluded as particles. This conclusion is corroborated by independent optical measurements. It is evident that the agreement between theory and experiments becomes progressively worse with increasing metal content and is virtually absent at $f_{exp} \gg 30$ vol. %. This can be understood as a result of a gradual breakdown of the separated-grain topology, and because multipole interactions between adjacent Co particles - which are not properly included in the Maxwell Garnett EMT - begin to play an important role.

The empirical data on $\bar{\varepsilon}$ can be used to optimize the solar selectivity. The parameters of concern are then the (normal) solar absorptance and the hemispherical thermal emittance. For illustrative purposes, we consider here the angular-dependent quantities, viz. A_{sol} (θ), which is obtained by averaging

$1-R(\theta,\lambda)$ over ϕ_{sol}, and $E_{therm}(\theta, 100°C)$, obtained by averaging $1-R(\theta,\lambda)$ over ϕ_{therm} pertaining to $\tau = 100°C$. Clearly $A_{sol}(\theta)$ should be as close to unity as possible and $E_{therm}(\theta, 100°C)$ should be as close to zero as possible. We carried out a detailed study of these latter quantities for $Co-Al_2O_3$ coatings of different thicknesses and compositions and laid on different substrate metals. The solar absorptance did not exceed ~ 85 % which is undesirably low, and hence an antireflection coating of Al_2O_3 was invoked in the design. After extensive optimization by computation

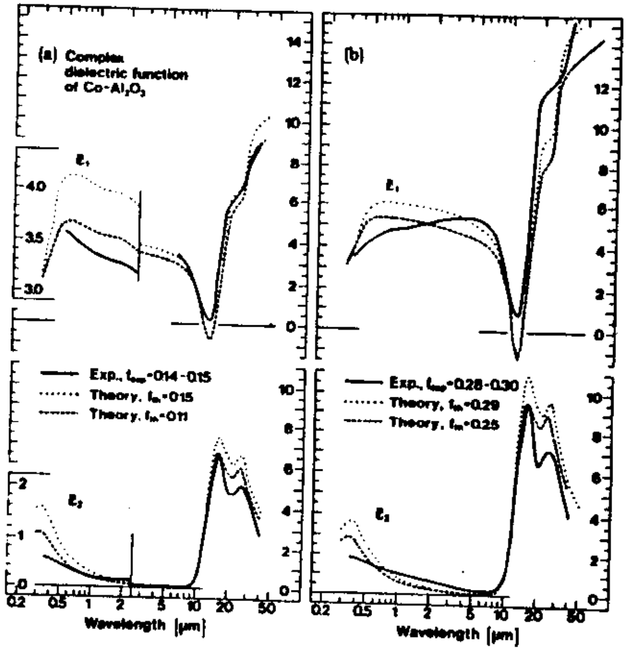

Figure 44. *Real and imaginary parts of the complex dielectric function of $Co-Al_2O_3$ coatings with different compositions in (a) and (b). Solid curves are based on measured data. Dashed and dotted curves are based on the Maxwell Garnett EMT.*

it was found that the optimum design was the following:
0.07 µm of $Co-Al_2O_3$ with $f_{exp} \approx 0.6$ antireflected with 0.07 µm of Al_2O_3 and laid on a transition-metal surface such as Ni. This configuration is shown in the inset of Fig. 45. Main part of this figure shows solar absorptance and thermal emittance as a function of angle of incidence; curves refer to computations based on measured $\bar{\varepsilon}$ and circles refer to evaluations based on spectral and angular dependent reflectance. The two sets of data are in good agreement. The peak of E_{therm} at large angles is due to the emission of p-polarised light. It is found that the solar

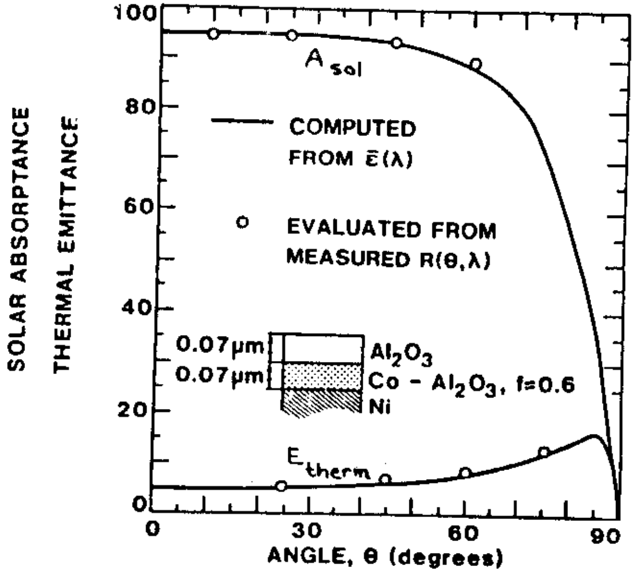

Figure 45. *Angular dependent solar absortance and thermal emittance as evaluated from reflectance data (circles) and as computed from dielectric permeabilities (solid curves) for the optimized two-layer coating sketched in the inset.*

absorptance is ~ 95 % for $\theta \leq 45^\circ$ and that E_{therm} is low. The hemispherical emittance is calculated to be ~ 7 %, whereas the corresponding value measured by microcalorimetry is ~ 9.5 %. Thus the spectral selectivity is very large.

6. MATERIALS FOR RADIATIVE COOLING TO LOW TEMPERATURES

6.1 The resource for radiative cooling

We first look back at Fig. 7c, which indicated that the atmospheric absorptance can be weak in the 8 - 13 - μm spectral range. The thermal radiation is strong at these wavelengths for objects at normal ambient temperature. If we consider a surface exposed to the sky, its emitted radiation does not have to be balanced by counterradiation, i.e., the surface can be spontaneously cooled. The magnitude of this source of cooling, the desired radiative surface properties (which are selective), and materials for thermal insulation of the radiatively cooled surfaces are covered below. Materials development for radiative cooling is a rather new research topic. No review has yet appeared, but references to earlier work can be found in Refs. 125 and 126.

The radiance coming from the atmosphere is extremely complicated.[127,128] The main gases, nitrogen and oxygen, contribute very little, whereas the variable constituents water vapour, carbon dioxide, ozone, and - to a much smaller extent - nitrogen oxides and hydrocarbons show important absorption bands in the thermal infrared wavelength range. Water vapour has a strong split vibrational band centered around 6.3 μm and also shows significant rotational absorption at $\lambda \gtrsim 20$ μm. This absorption can extend to shorter wavelength if the humidity is high. Carbon dioxide has a broad intensive vibrational band centered at ~ 15 μm. Ozone absorption is not equally important but several absorption bands lie in the infrared. Most of these are masked by water vapour and carbon dioxide, but a narrow absorption band at 9.6 μm shows up distinctly. One concludes that the atmospheric downward radiation shows two important features. First, the spectral radiance has a minimum in an interval which lies between the major absorption bands of water vapour and carbon dioxide, as we have already noted. Second, the overall spectral radiance depends strongly on climatic conditions - particularly on the amount of water vapour. These features have been verified by direct measurements.

For quantitative assessments of the cooling resource, it is useful to start from detailed data on the spectral sky radiance representative of typical climates at different latitudes. Such results can be extracted from a computer program known as[129] LOWTRAN 5. It uses a single parameter band model for the molecular absorption and includes the effects of continuum absorption, molecular scattering, and aerosol extinction. Atmospheric refraction and earth curvature are included for slant atmospheric paths. For radiative cooling purposes, the LOWTRAN 5 program needs to be used exclusively in the radiance mode, in which a numerical evaluation of the integral form of the radiative transfer equation is employed. The emission from aerosols and the treatment of aerosol and molecular scattering are considered only to zeroth order; additional contributions to atmosperic emission from scattered radiation are neglected. Local thermodynamic equilibrium is assumed. The radiance data obtained from LOWTRAN are know to be in a very good overall agreement with measured results.

The LOWTRAN 5 program is provided with data for five seasonal model atmospheres together with the 1962 U.S. standard atmosphere. It is also possible to replace these by user derived or measured values. The seasonal models are representative of the following atmospheres:
tropical (15°N), midlatitude summer (45°N, July), midlatitude winter (45°N, January) subarctic summer (60°N, July), and subarctic winter (60°N, January). The atmospheres are specified in terms of height profiles for temperature, barometric pressure, and densities of water vapour, ozone, nitric acid, and of the uniformly mixed gases (CO_2, N_2O, CH_4, CO, N_2 and O_2). The LOWTRAN 5 code also contains several aerosol models.

Figure 46 shows atmospheric radiance for all six model atmospheres, as obtained from the LOWTRAN 5 program. The data are reproduced from Ref. 130. These curves are seen to drop below, or to follow approximately, the blackbody radiance spectra for temperatures chosen to correspond to those of the lowest kilometer of the various atmospheres (denoted by τ_a) for frequencies above 350 cm^{-1}. At lower frequencies, where no LOWTRAN data are available, only the blackbody curve is plotted. We find for all atmospheres that the actual radiance lies far below that of the blackbody in the 8-13 µm range (known as the "atmospheric window"). A secondary window at 16-22 µm is of much smaller importance. The emittance in the atmospheric window goes up with increasing zenith angle.

We now turn to quantitative predictions of cooling power and achievable temperature difference. The net radiative flux from a surface which faces the sky is obtained as the difference between outgoing and incoming contributions according to[125]

$$P_{rad} = \pi\int_0^{\pi/2} d(\sin^2\theta)\int_0^{\infty} d\lambda[1-R(\theta,\lambda)]\ [\phi_{therm}(\lambda,\tau_s) - \phi_{atm}(\theta,\lambda)], \qquad (46)$$

where $R(\theta,\lambda)$ refers to the radiating surface whose temperature is τ_s and $\phi_{atm}(\theta,\lambda)$ is the radiance for either of the model atmospheres. Thus $\phi_{atm}(\theta,\lambda)$ is obtained from the LOWTRAN 5 program for $\lambda < 28.6 \mu m$, whereas $\phi_{atm}(\theta,\lambda) = \phi_{therm}(\lambda,\tau_a)$ above this wavelength. The difference between the ambient and the surface temperature is denoted by ΔT, i.e.,

$$\Delta T = \tau_a - \tau_s \qquad (47)$$

For $\Delta T > 0$ it is necessary to consider the role of a nonradiative heat influx to the radiating surface. The practically useful cooling power P_c is then

$$P_c = P_{rad} - \kappa\Delta T, \qquad (48)$$

where the loss is specified in terms of a linear heat-transfer coefficient κ.

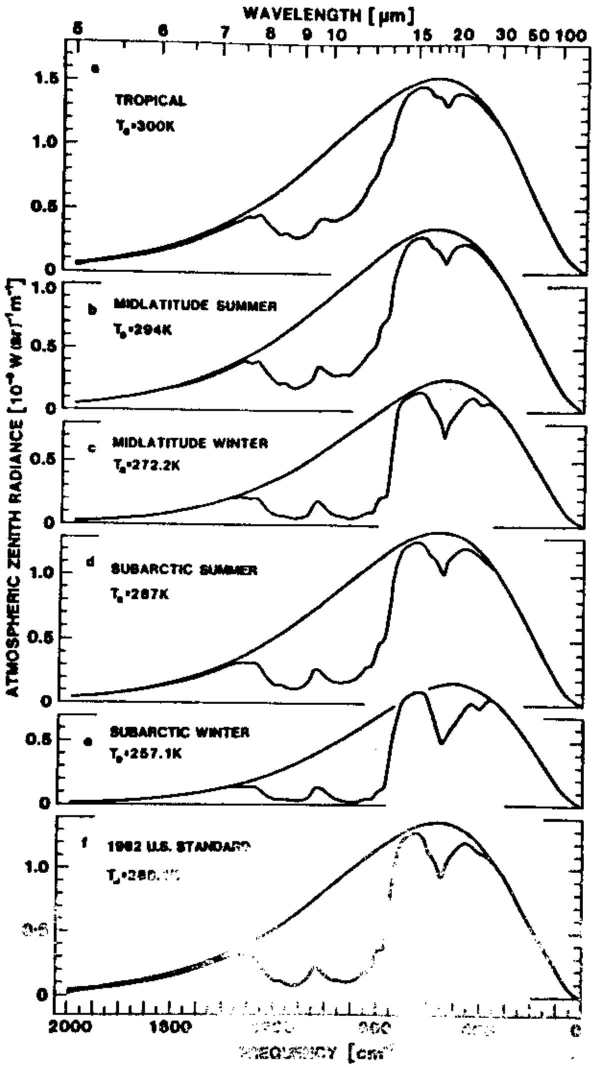

Figure 46. *Spectral zenith radiance and corresponding blackbody radiance for six model atmospheres, as computed from the LOWTRAN 5 model.*

As seen from Eq. (46), the radiative flux depends strongly on the absorptance (or, equivalently, the emittance) of the radiating surface, i.e., on the (1-R) factor. We now consider three cases. The first of these regards a blackbody radiator defined by

$$R(\theta,\lambda) = 0. \tag{49}$$

This surface experiences the largest cooling power at ambient temperature. Blackbodies serve as a good approximation for organic matter, soils, rocks, water, concrete, asphalt, ordinary uncoated glass, etc. The second case is *the selectively infrared emitting surface* designed for achieving the lowest possible temperature. This surface should have high emittance in the 8-13-μm atmospheric window range, where the counter radiation is weak, and low absorptance outside this interval, so that the main portion of the radiation from H_2O and CO_2 is not interacting with the surface. Hence the ideal property is

$$R(\theta,\lambda) = R_{sel}(\theta,\lambda) = 0 \quad \text{for } 8 \leq \lambda \leq 13 \ \mu\text{m}, \tag{50}$$

$$= 1, \text{ elsewhere}. \tag{51}$$

In Sec. 6.2. below we discuss practical surfaces which approximate this ideal property. The third case is the metallic surface with, ideally, $R(\theta,\lambda) = 1$. Now $P_{rad} = 0$, i.e. no radiative cooling occurs.

Figure 47 shows calculated results of P_{rad} as a function of ΔT. The data apply to surfaces which radiate freely toward model atmospheres of the six types earlier discussed. In Fig. 47 (a) the radiating surface is taken to be a blackbody; in Fig. 47 (b) it has an ideal infrared-selective characteristic according to Eqs. (50) and (51). For both cases, the incoming power is governed by the hemispherical radiance. It is found that the radiative cooling power at ambient temperature lies between 71 and 113 Wm^{-2} for the blackbody surface and between 58 and 93 Wm^{-2} for the infrared-selective surface. The largest powers hold for U.S. STD and the lowest for TROP.

The values for the infrared-selective surface lie below those for the blackbody surface since only the latter takes advantage of the nonzero magnitude of (ϕ_{therm} - ϕ_{atm}) outside the 8-13-μm interval (cf. Fig. 46).

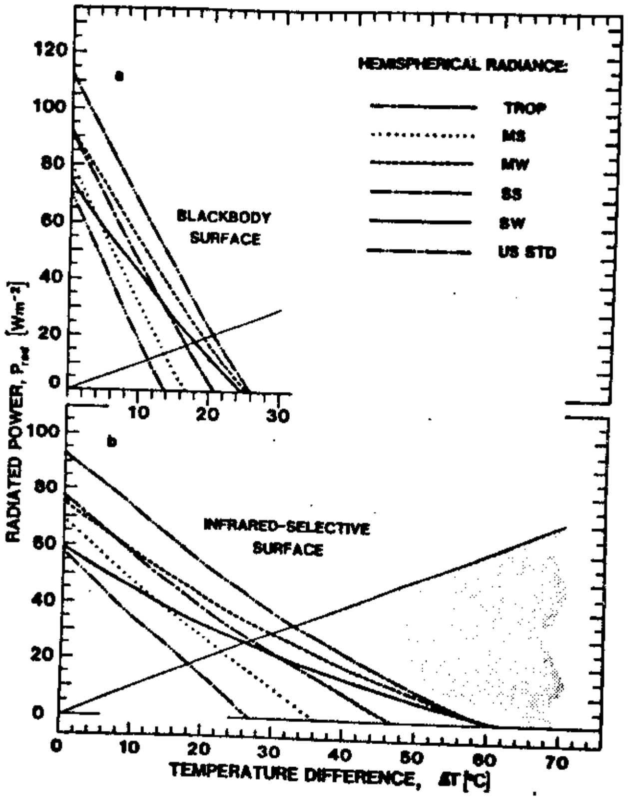

Figure 47. Calculated relation between radiative cooling power and temperature difference for six model atmospheres (cf. Fig. 46) and two ideal surfaces.

The radiative cooling power is seen to decrease monotonically with increasing ΔT. The decrease is much slower for the infrared-selective surface than for the blackbody surface, since the former employs radiation balance only in the 8-13-μm range where the atmospheric radiance is weak. It is seen that ultimate temperature differences between 14 and 26°C for the blackbody surface and between 27 and 62°C for the infrared-selective surface are predicted. Such large ΔTs cannot be obtained in practice, though, but the role of conductive and convective losses of cooling power must be included by use of a nonzero heat transfer coefficient. As a practical low limit obtainable by use of an efficient infrared-transparent convection shield we set $\kappa = 1\ Wm^{-2}\ K^{-1}$. We return to this point in Sec. 6.3. This requirement makes the shaded triangular areas in Fig. 47 inaccessible for a cooling device. It is seen from the figure that temperature differences between 11 and 21°C for the blackbody surface and between 18 and 33°C for the infrared-selective surface are expected with $\kappa = 1\ Wm^{-2}\ K^{-1}$. Again the higher values pertain to U.S. STD and the lower to TROP. Analogous computations for exchange only with the zenith atmospheric radiation are found in Ref. 130. Some improvement of the radiative cooling performance can be obtained under such conditions.

6.2 Materials with infrared-selective emission

It is apparent that surfaces which are infrared-selective according to Eqs. (50) and (51) have a potential for reaching considerably lower temperatures than non-selective surfaces. This ideal spectral profile is indicated by the dotted lines in Fig. 48. Low temperatures are of importance for applications related to the preservation of nutrients, vaccins, etc., as well as for many other important applications. This section is devoted to different types of infrared-selective surfaces.

The first approach regards thin *inorganic coatings* backed by reflecting metal. Particularly good results have been obtained by use of silicon oxynitride. Coatings of this kind can be prepared by a variety of techniques. In our own work[131] we used e-beam deposition of Si_3N_4 under slightly reactive conditions as well as reactive rf magnetron sputtering of Si.[132] Figure 48 shows spectral reflectance for a 1.34-μm thick e-beam deposited film of $SiO_{0.6}N_{0.2}$ on Al. The composition was determined by Rutherford backscattering spectrometry. The curves refer to 45° angle of incidence of polarised light.

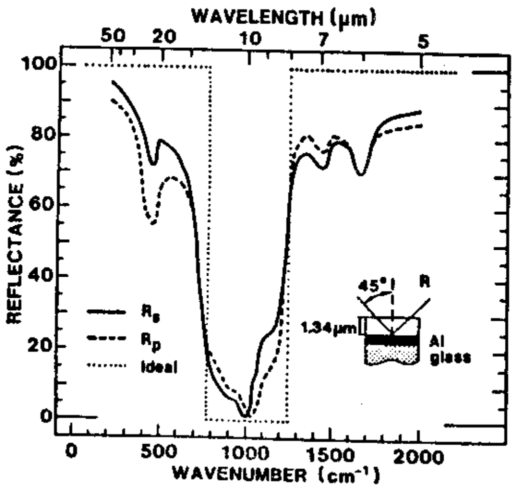

Figure 48. *Spectral reflectance for a film of* $SiO_{0.6}N_{0.2}$ *deposited onto Al. Dotted lines indicate the ideal spectral profile.*

The low reflectance in the 8-13-μm wavelength range, and the high reflectance elsewhere, proves that the right kind of infrared selectivity prevails.

For optimization purposes, it is convenient to define two parameters which govern the essential features of the radiative cooling performance of a material with known infrared-optical properties. These parameters can be viewed as the counterpart of the pair of parameters which characterizes the selectively solar-absorbing surface designed for optimum photothermal conversion - viz. the solar absorptance and thermal emittance discussed above. We first observe (cf. Fig. 46) that the atmospheric radiance deviates significantly from the blackbody curve only in the 8-13-μm interval. It is then approximately correct to set the atmospheric emittance equal to a low and constant value for 8-13-μm and equal to unity elsewhere. This "box model" for the atmospheric radiation then leads naturally to integrated surface emittance values according to[125]

$$\bar{e}_s^H \equiv E_{therm}, \qquad (52)$$

$$\bar{e}_{s2}^H \equiv \int_{8\mu m}^{13\mu m} d\lambda\, \Phi_{therm}(\lambda,\tau_a)\left[1 - R_h(\lambda)\right] \Big/ \int_{8\mu m}^{13\mu m} d\lambda\, \Phi_{therm}(\lambda,\tau_a), \qquad (53)$$

$$\eta^H \equiv \bar{e}_{s2}^H / \bar{e}_s^H, \qquad (54)$$

where we have chosen to keep the notation of Ref. 125. Essentially, $\bar{e}_{s2}^H$ governs the cooling power at ambient temperature and η^H governs the maximum achievable temperature drop. Efficient cooling requires a large value - ideally unity - of $\bar{e}_{s2}^H$, and if low temperatures are to be reached we also require a large magnitude of η^H. The theoretical maximum of the latter quantity is 3.39 at $\tau_a = 0^oC$.

Figure 49 shows the basic cooling parameters at $\tau_a = 0^oC$ for silicon oxynitride and for silicon monoxide backed by Al. The computations used as input the complex dielectric functions of the two materials (determined according to the techniques outlined in Sec. 2.4). It is found that silicon oxynitride layers with thicknesses in the 1-2-μm range have very good properties for radiative cooling. Practical tests with such coatings have given ΔT ≈ 20°C under favourable conditions.

A second approach to selective infrared emission is offered by *polymer coats* on metal backings. Polyvinylfluoride (also known as Tedlar) has been popular.

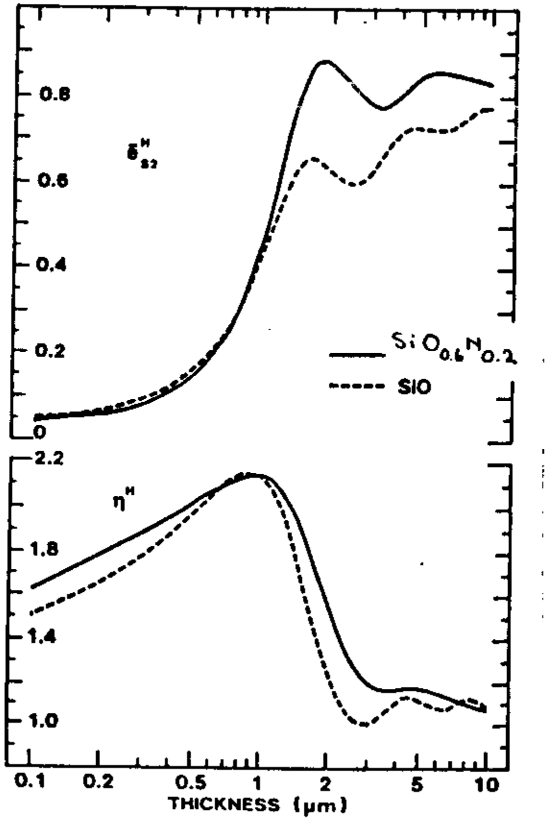

Figure 49. Basic cooling parameters as computed for silicon oxynitride and silicon monoxide.

A third approach utilizes *slabs of selectively infrared emitting gases* confined by infrared-transparent foils and backed by metal. The gases of interest are ammonia, ethylene, ethylene oxide, and mixtures of the latter two. Their radiative properties can be understood from the molecular configurations.[133]

Figure 50 shows infrared transmission spectra for NH_3 withthree different pathlengths and at normal pressure. The gas cells were tubes with two 13-μm-thick polyethylene windows. The upper graphs in Figs. 50 (a) - (c) indicate the transmittance through air-filled cells. The two narrow minima stem from absorption in the polyethylene. The lower graphs in Figs. 50 (a) - (c) were recorded with gas-filled cells. The differences among the pairs of curves (shaded areas) show that NH_3 displays a broad absorption band covering the desired 8-13-μm interval forpathlengths exceeding ∿ 1 cm. The interesting absorption is centered around an infrared active fundamental at the frequency 950 cm^{-1}. The corresponding vibration can be visualized as the N atom moving perpendicular to the H_3 plane of the ammonia molecule while its pyramidal configuration is retained. This fundamental undergoes broadening as a result of several mechanisms including inversion doubling, rotation (i.e., quantization of the angular momentum), centrifugal deformation, and pressure effects. It is seen from Fig. 50 that the absorption becomes too high at the largest pathlengths and, in particular, a strong absorption due to a thermal population of free-roational levels sets in at the far-infrared end of the spectrum. Data on C_2H_4 and C_2H_4O can be given analogous interpretations.[133]

The transmittance data for the three gases were used to derive spectral absorptance coefficients, from which we obtained the basic cooling parameters in principally the same way as for the thin solid films. Figure 51 shows $\bar{e}^H_{s2}$ and η^H for gas slabs of thicknesses between 0.1 and 50 cm. The

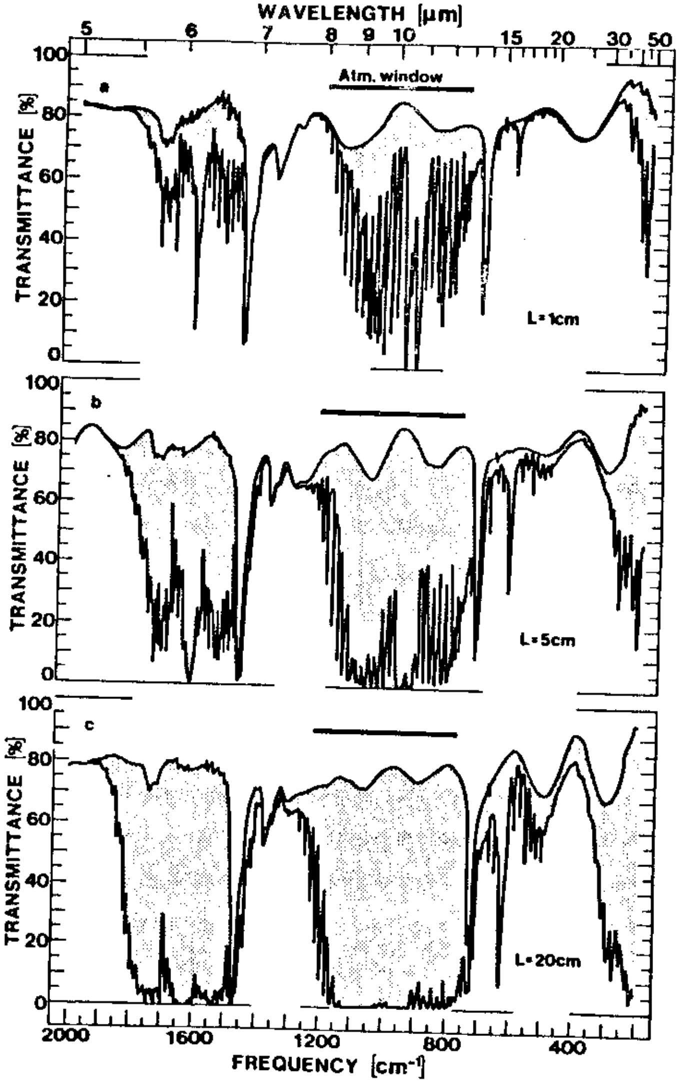

Figure 50. Spectrophotometric transmittance for NH_3 gas at normal pressure as measured with cells having the shown lengths, L.

slabs are thought to be backed by Al. It is seen that for gas layers thicker than ∿ 1 cm, the cooling power at ambient temperatures is larger for NH_3 than for the hydrocarbon gases. However, η^H is larger for C_2H_4 and C_2H_4O than for NH_3 implying that the hydrocarbons display a higher degree of spectral selectivity. Gas mixtures are also of interest. These are discussed elsewhere.[133] Field tests of radiative gas cooling have yielded temperature differences as large as 8.5°C in full daylight.

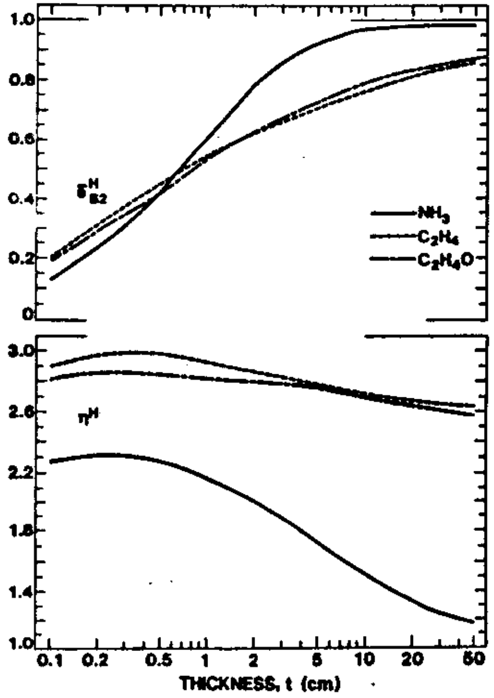

Figure 51. Basic cooling parameters for NH_3, C_2H_4, and C_2H_4O gas layers of different thicknesses.

6.3 Infrared-transparent convection shields (Ref. 134)

Low temperatures can be produced by radiative cooling *only* if the thermal coupling between the radiating surface and the ambient air is weak. This was illustrated by Fig. 47; clearly the non-radiative heat-transfer coefficient must be small (or the non-radiative thermal resistance be high) in order to obtain high cooling power and large temperature difference. This calls for a new type of material which *combines high infrared transmittance with high non-radiative heat resistance.* In earlier work known to us, simple polyethylene foils have been used for this purpose. This would be an adequate approach for radiative cooling devices placed in still air. However, in practice the flexible foils are moved by winds and forced convection tends to deteriorate the cooling performance. One solution to this problem is to construct the convection shield so that it comprises cells which are sufficiently minute that air convection is insignificant. In practice, the cell size should be $\lesssim 1$ cm.[135]

We have recently investigated a new type of infrared-transparent convection shield designed for radiative cooling.[134] It is constructed from crossed layers of vee-corrugated high-density polyethylene foil. The individual layers are made by hot-forming. The design is sketched in Fig. 52. The samples studied so far have h equal to 0.5, 1 and 1.5 cm and θ equal to 90^0 or 45^0.

The infrared transmittance through the material was determined by use of the experimental arrangement shown in the inset of Fig. 53. The sample is placed closely in front of a blackbody-like radiator and is viewed by infrared-imaging equipment. This type of measurement enabled us to evaluate the transmittance as a function of the number of individual foils. Filled circles and open triangles in Fig. 53 pertain to corrugated foils with

different apex angles. The transmittance goes monotonically from ∿ 90 % for a single foil to ∿ 60 % for five foils, which is the expected behaviour. Data for flat foils, indicated by open squares, are in acceptable agreement with spectrophotometric recordings. It is found from Fig. 53 that the transmittance is higher for corrugated foils than for flat ones; this is corroborated by recent literature data.[136]

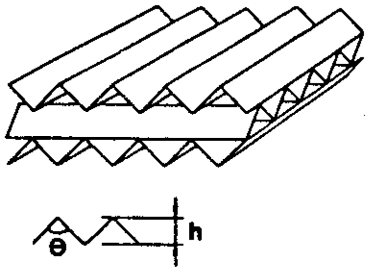

Figure 52. Sketch of a novel infrared-transparent convection shield for radiative cooling applications.

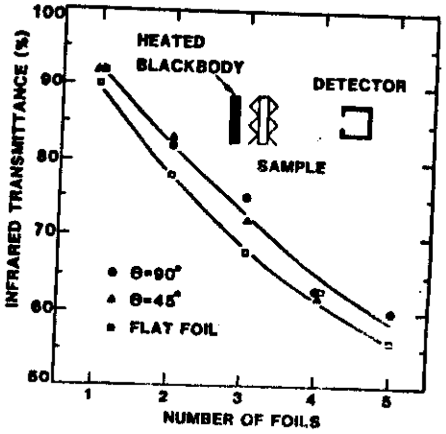

Figure 53. Transmittance in the 8-13-µm range vs. number of polyethylene foils for different sample geometries.

The non-radiative thermal resistance was measured by a modification of the well known guarded hot-plate techniqe. The inset of Fig. 54 shows the essential features of this technique. Highly reflecting Al foil was attached to the plates in order to minimize direct radiative coupling between them. Figure 54 shows non-radiative thermal resistance as a function of sample thickness. The data for corrugated foils yield a consistent pattern with a monotonically varying thermal resistance lying below the values for empty air gaps. Heat flow through partially transparent materials is complicated, and the shown data is not readily amenable to theoretical modeling.

Looking at Figs. 53 and 54, it is evident that an increase of the thermal resistance is accompanied by a decrease of the infrared transmittance. With regard to radiative cooling applications, there is thus a trade-off between the two properties. As a characteristic result we find that at a thickness of 4.5 cm - corresponding to three 1.5 cm-thick corrugated foils - the thermal resistance is 1.1 m^2KW^{-1} and the infrared transmittance is 73 %.

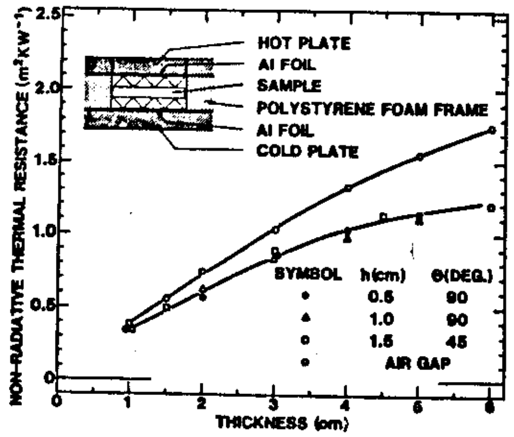

Figure 54. Non-radiative thermal resistance vs the thickness for different sample geometries.

REFERENCES

1. C.G. Granqvist, Appl. Opt. 20, 2606 (1981).
2. C.M. Lampert, Proc. SPIE 324, 1 (1982).
3. C.G. Granqvist, Proc. SPIE 401, 330 (1983).
4. C.M. Lampert, Opt. Engr. 23, 92 (1984).
5. C.G. Granqvist, The Physics Teacher 22, 372 (1984).
6. C.G. Granqvist, Physica Scripta 32, 401 (1985).
7. O.S. Heavens, *Optical Properties of Thin Solid Films* (Butterworth, London, 1955).
8. M. Born and E. Wolf, *Principles of Optics*, 6th edition (Pergamon Oxford, 1980).
9. G.D. Mahan, *Many Particle Physics* (Plenum, New York, 1981).
10. R. Landauer, AIP Conf. Proc. 40, 2 (1978).
11. A.J. Sievers, in *Solar Energy Conversion: Solid State Physics Aspects*, Vol. 31 of *Topics in Applied Physics*, edited by B.O. Seraphin (Springer, Berlin, 1979); p. 57.
12. C.G. Granqvist, J. Phys. (Paris) 42, C1-247 (1981).
13. D.E. Aspnes, Am. J. Phys. 50, 704 (1982); Thin Solid Films 89, 249 (1982).
14. G.A. Niklasson and C.G. Granqvist, in *Contributions of Clusters Physics to Materials Science and Technology*, edited by J. Davenas and P. Rabette (Martinus Nijhoff, Dordrecht, 1986).
15. M. Kerker, *The Scattering of Light and Other Electromagnetic Radiation* (Academic, New York, 1969).
16. H.C. van de Hulst, *Light Scattering by Small Particles* (Dover, New York, 1981).
17. C.F. Bohren and D.R. Huffman, *Absorption and Scattering by Small Particles* (Wiley, New York, 1983).

18. J.C.M. Garnett, Philos. Trans. Roy. Soc. London 203, 385 (1904); 205, 237 (1906).

19. D.A.G. Bruggeman, Ann. Phys. (Leipzig) 24, 636 (1935).

20. G.A. Niklasson and C.G. Granqvist, J. Appl. Phys. 55, 3382 (1984).

21. D.J. Bergman, in *Macroscopic Properties of Disordered Media*, Vol. 154, in *Lecture Notes in Physics*, edited by R. Burridge, C. Childress and G. Papanicolaou (Springer, Berlin, 1982); p. 10.

22. D.J. Bergman, Ann. Phys. (NY) 138, 78 (1982).

23. A. Hjortsberg, Appl. Opt. 7, 1254 (1981).

24. E.D. Palik (editor), *Handbook of Optical Constants* (Academic, New York, 1985).

25. G. Wyszecki and W.S. Stiles, in *Color Science, 2nd edition* (Wiley, New York, 1982) p. 256.

26. M.P. Thekaekara, in *Solar Energy Engineering*, edited by A.A.M. Sayigh (Academic, New York, 1977), p. 37.

27. E. Ritter, in *Progr. Electro-Optics*, edited by E. Camatini (Plenum, New York, 1975); p. 181.

28. S.M. Berman and S.D. Silverstein, editors, AIP Conf. Proc. 25, 286 (1975).

29. J.C.C. Fan and F.J. Bachner, Appl. Opt. 15, 1012 (1976).

30. J.L. Vossen, Phys. Thin Films 9, 1 (1977).

31. G. Haacke, Ann. Rev. Mater. Sci. 7, 73 (1977).

32. C.M. Lampert, Solar Energy Mater. 6, 1 (1981).

33. C.M. Lampert, Ind. Chem. Prod. Res. Rev. 21, 612 (1982).

34. H. Köstlin, Festkörperprobleme 22, 229 (1982).

35. G. Haacke, Proc. SPIE 324, 10 (1982).

36. J.C. Manifacier, Thin Solid Films 90, 297 (1982).

37. Z.M. Jarzebski, Phys. Stat. Sol. A 71, 13 (1982).

38. G. Frank, E. Kauer, H. Köstlin and F.J. Schmitte, Proc. SPIE 324, 58 (1982).

---

39. C.M. Lampert, Energy Res. 7, 359 (1983).

40. P.H. Berning, Appl. Opt. 22, 4127 (1983).

41. K.L. Chopra, S. Major and D.K. Pandya, Thin Solid Films 102, 1 (1983).

42. E. Valkonen, B. Karlsson and C.-G. Ribbing, Solar Energy 32, 211 (1984).

43. C.G. Granqvist, I. Hamberg and J.S.E.M. Svensson, Ind. Chem. Prod. Res. Dev. 24, 93 (1985).

44. C.M. Lampert, Solar Energy Mater. 11, 1 (1984).

45. G.B. Smith, G.A. Niklasson, J.S.E.M. Svensson and C.G. Granqvist, J. Appl. Phys. 59, 571 (1986).

46. K.L. Chopra, *Thin Film Phenomena* (McGraw-Hill, New York, 1969).

47. C.A. Neugebauer, in *Handbook of Thin Film Technology*, edited by L.I. Maissel and R. Glang (McGraw-Hill, New York, 1970), Ch. 8.

48. G.L. Harding, Solar Energy Mater. 12, 169 (1985).

49. G.L. Harding, I. Hamberg and C.G. Granqvist, Solar Energy Mater. 12, 187 (1985).

50. H. Gugg . M. Jurich, J.D. Swalen and A.J. Sievers, Phys. Rev. B30, 4189 (1984).

51. S. Norrman, T. Andersson, C.G. Granqvist and O. Hunderi, Phys. Rev. B18, 67 (1978).

52. T.S. Eriksson, S.-J. Jiang and C.G. Granqvist, Appl. Opt. 24, 745 (1985).

53. I. Hamberg, A. Hjortsberg and C.G. Granqvist, Appl. Phys. Lett. 40, 362 (1982); Proc. SPIE 324, 31 (1982).

54. I. Hamberg and C.G. Granqvist, Appl. Opt. 22, 609 (1983).

55. I. Hamberg and C.G. Granqvist, Thin Solid Films 105, L 83 (1983).

56. I. Hamberg and C.G. Granqvist, Proc. SPIE 428, 2 (1983); Appl. Phys. Lett. 44, 721 (1984).

57. I. Hamberg, C.G. Granqvist, K.-F. Berggren, B.E. Sernelius and L. Engström, Phys. Rev. B 30, 3240 (1984); Proc. SPIE 502, 2 (1984).

58. I. Hamberg and C.G. Granqvist, Appl. Opt. 24, 1815 (1985); Proc. SPIE 562, to be published.

59. I. Hamberg and C.G. Granqvist, J. Appl. Phys., to be published.

60. R.P. Howson, M.I. Ridge and K. Suzuki, Proc. SPIE 428, 14 (1983), and references therein.

61. S.-J. Jiang and C.G. Granqvist, Proc. SPIE 562, to be published.

62. A.C. Hardy, *Handbook of Colorimetry* (Massachusetts Institute of Technology, Cambridge, 1963).

63. F. Grum and C.J. Bartleson (editors), *Optical Radiation Measurements, Vol. 2, Color Measurement* (Academic, New York, 1980).

64. D.L. MacAdam, *Color Measurement: Theme and Variations* (Springer, Berlin, 1981).

65. N.F. Mott, *Metal-Insulator Transitions* (Taylor and Francis, London, 1974).

66. E. Burstein, Phys. Rev. 93, 632 (1954); T.S. Moss, Proc. Phys. Soc. London B 67, 775 (1954).

67. M.V. Kurik, Phys. Stat. Sol. A8, 9 (197[illegible].

68. D. Redfield, Phys. Rev. 130, 914, 916 (1963).

69. T. Skettrup, Phys. Rev. B18, 2622 (1978).

70. E. Gerlach and P. Grosse, Festkörperprobleme 17, 157 (1977).

71. G. Frank and H. Köstlin, Appl. Phys. A 27, 197 (1982).

72. J. Lindhard, Kgl. Danske Videnskab. Selskab, Mat.-Fys. Medd. 28, No. 8 (1954).

73. J. Hubbard, Proc. Roy. Soc. London, Ser. A. 243, 336 (1957).

74. H. Köstlin, R. Jost and W. Lems, Phys. Stat. Sol. A 29, 87 (1975).

75. W.B. White and V.G. Keramidas, Spectrochim. Acta 28A, 501 (1972).

76. B.W. Faughnan and R.S. Crandall, in *Display Devices*, edited by J.I. Pankove, *Topics in Applied Physics*, Vol. 40 (Springer-Verlag, Berlin, Heidelberg, 1980), p. 181.

77. G. Beni and J.L. Shay, Adv. Image Pickup and Display 5, 83 (1982).

78. W.C. Dautremont-Smith, Displays, January 1982, p. 3; April 1982, p. 72.

79. J.S.E.M. Svensson and C.G. Granqvist, Proc. SPIE 502, 30 (1984); Solar Energy Mater. 12, 391 (1985).

80. J.S.E.M. Svensson and C.G. Granqvist, Appl. Phys. Lett. 45, 828 (1984).

81. R.B. Goldner, D.H. Medelsohn, J. Alexander, W.R. Hendersson, D. Fitzpatrick, T.E. Haas, H.H. Sample, R.D. Rauh, M.A. Parker and T.L. Rose, Appl. Phys. Lett. 43, 1039 (1983), R.B. Goldner and R.D. Rauh, Proc. SPIE 428, 38 (1983); Solar Energy Mater. 11, 177 (1984).

82. R.B. Goldner, P. Norton, K. Wong, G. Foley, E.L. Goldner, G. Seward and R. Chapman, Appl. Phys. Lett. 47, 536 (1985).

83. J.S.E.M. Svensson and C.G. Granqvist, Solar Energy Mater. 11, 29 (1984).

84. J.S.E.M. Svensson and C.G. Granqvist, Thin Solid Films 126, 31 (1985).

85. C.M. Lampert, T.R. Omstead and P.C. Yu, Proc. SPIE 562 (1985), to be published.

86. J.S.E.M. Svensson and C.G. Granqvist, to be published.

87. P. Oliva, J. Leonardi, J.F. Laurent, C. Delmas, J.J. Braconnier, M. Figlarz, F. Fievet and A. de Guibert, J. Power Sources 8, 229 (1982).

88. G. Jorgenson, Lawrence Berkeley Laboratory Report LBL - 18299 (August 1984).

89. S.M. Babulanam, unpublished.

90. A.B. Meinel and M.P. Meinel, *Applied Solar Energy: An Introduction* (Addison-Wesley, Reading, 1976); Ch. 9.

91. B.O. Seraphin and A.B. Meinel, in *Optical Properties of Solids - New Developments*, edited by B.O. Seraphin (North-Holland, Amsterdam, 1976); Ch. 17.

92. R.E. Hahn and B.O. Seraphin, Phys. Thin Films 10, 1 (1978).

93. B.O. Seraphin, in *Solar Energy Conversion: Solid State Physics Aspects*, Vol. 31 of *Topics in Applied Physics*, edited by B.O. Seraphin (Springer, Berlin, 1979); p. 5; in *Solar Energy Conversion: An Introductory Course*, edited by A.E. Dixon and J.D. Leslie (Pergamon, New York, 1979), p. 287.

94. C.M. Lampert, Solar Energy Mater. 1, 319 (1979); 2, 1 (1979).

95. P.K. C. Pillai and R.C. Agarwal, Phys. Stat. Sol. A60, 11 (1980).

96. O.P. Agnihotri and B.K. Gupta, *Solar Selective Surfaces* (Wiley, New York, 1981).

97. M.M. Koltun, *Selektivnye Opticheskie Poverkhnosti Preobrazovatelei Solnechnoi Energii* (Nauka Press, Moscow, 1979). English translation: *Selective Optical Surfaces for Solar Energy Converters* (Allerton Press, New York, 1981).

98. S.A. Herzenberg and R. Silberglitt, Proc. SPIE 324, 92 (1982).

99. W.F. Bogaerts and C.M. Lampert, J. Mater. Sci. 18, 2847 (1983).

100. G.A. Niklasson and C.G. Granqvist, J. Mater. Sci. 18, 3475 (1983).

101. E. Randich and D.D. Allred, Thin Solid Films 83, 393 (1981); E. Randich and R.B. Pettit, Solar Energy Mater. 5, 425 (1981).

102. B.O. Seraphin, Thin Solid Films 39, 87 (1976); 57, 293 (1979).

103. M. Janai, D.D. Allred, D.C. Booth and B.O. Seraphin, Solar Energy Mater. 1, 11 (1979).

104. D.C. Booth, D.D. Allred and B.O. Seraphin, Solar Energy Mater. 2, 107 (1979).

105. J.A. Thornton and J.L. Lamb, Thin Solid Films 96, 175 (1982).

106. See entries 321-408 in Ref. 100, as well as several articles in Vols. 6-12 of Solar Energy Mater.

107. S.N. Patel and O.T. Inal, Thin Solid Films 113, 50 (1984).

108. A. Andersson, O. Hunderi and C.G. Granqvist, J. Appl. Phys. 51, 754 (1980).

109. E.E. Chain, K. Seshan and B.O. Seraphin, J. Appl. Phys. 52, 1356 (1981).

110. G.A. Niklasson and C.G. Granqvist, J. Appl. Phys. 55, 3382 (1984).

111. G.D. Pettit, J.J. Cuomo, T.H. Di Stefano and J.M. Woodall, IBM J. Res. Dev. 22, 372 (1978).

112. G.L. Harding and M.R. Lake, Solar Energy Mater. 5, 445 (1981).

113. P.M. Driver and P.G. McCormick, Solar Energy Mater. 6, 159, 381 (1982).

114. G.E. McDonald, Solar Energy 17, 119 (1975).

115. H.Y.B. Mar, R.E. Peterson and P.B. Zimmer, Thin Solid Films 39, 95 (1976).

116. P.M. Driver, R.W. Jones, C.L. Riddiford and R.J. Simpson, Solar Energy 9, 301 (1977).

117. J.C.C. Fan and S.A. Spura, Appl. Phys. Lett. 30, 511 (1977).

118. J.J. Mason, Proc. SPIE 324, 139 (1982).

119. P.K. Gogna, K.L. Chopra and S.C. Mullick, Energy Res. 4, 317 (1980).

120. S. Craig and G.L. Harding, Thin Solid Films 101,97 (1983).

121. A. Roos, B. Karlsson and T. Chibuye, Solar Energy Mater. 7, 453 (1983); A. Roos and B. Karlsson, Solar Energy Mater. 7, 467 (1983).

122. J.J. Mason, Proc. SPIE 428, 159 (1983).

123. Entries 474 - 494 in Ref. 100.

124. S.W. Moore, Proc. SPIE 324, 148 (1982).

125. C.G. Granqvist and A. Hjortsberg, J. Appl. Phys. 52, 4205 (1981).

126. T.S. Eriksson, E.M. Lushiku and C.G. Granqvist, Proc. SPIE 428, 105 (1983).

127. K. Ya. Kondratyev, *Radiation in the Atmosphere* (Academic, New York, 1969).

128. V.E. Zuev, *Propagation of Visible and Infrared Radiation in the Atmosphere* (Wiley, New York, 1974).

129. F.X. Kneizys, E.P. Shettle, W.O. Gallery, J.H. Chetwynds, Jr., L.W. Abreu, J.E.A. Selby, R.W. Fenn, and R.A. McClatchey, *Atmospheric Transmittance/Radiance Computer Code LOWTRAN 5*, Air Force Geophysics Laboratory, Technical Report AFGL-TR-80-0067 (February 1980).

130. T.S. Eriksson and C.G. Granqvist, Appl. Opt. 21, 4381 (1982).

131. T.S. Eriksson and C.G. Granqvist, Appl. Opt. 22, 3204 (1983).

132. T.S. Eriksson and C.G. Granqvist, to be published.

133. E.M. Lushiku and C.G. Granqvist, Appl. Opt. 23, 1835 (1984).

134. N.A. Nilsson, T.S. Eriksson and C.G. Granqvist, Solar Energy Mater. 12, 327 (1985).

135. F. Kreith, *Principles of Heat Transfer*, third edition (Intext, New York, 1973).